UNIVERSITÀ DEGLI STUDI DI PADOVA

DIPARTIMENTO DI BIOLOGIA

Corso di Laurea in Biologia Molecolare

ELABORATO DI LAUREA

Analisi longitudinale di dati di RNA-seq a singola cellula per lo studio della chemioresistenza nel cancro ovarico metastatico

Tutor: Prof.ssa Chiara Romualdi

Dipartimento di Biologia

Laureanda: Elena Cibola

ANNO ACCADEMICO 2021/2022

Indice

Abstract

Ai pazienti con carcinoma ovarico sieroso di alto grado (HGSOC) viene solitamente prescritta una chemioterapia a base di platino. Tuttavia, la maggior parte dei soggetti con questa patologia sviluppa resistenza a tale trattamento e quindi si ritrova ad avere un tumore refrattario fatale.

L'obiettivo dell'articolo di Kaiyang Zhang *et al.*, presentato e discusso in questo elaborato, è definire uno stato cellulare resistente alla chemioterapia nel HGSOC, grazie al quale possono essere identificati biomarcatori, utilizzabili per effettuare previsioni sulla chemioresistenza, e possibili bersagli per superarla.

Gli autori hanno raccolto campioni di tessuto prima e dopo la chemioterapia da 11 pazienti con HGSOC e hanno misurato i loro profili trascrittomici mediante RNA-seq a singola cellula (scRNA-seq). Per permettere il confronto tra campioni diversi, hanno rimosso i segnali paziente-specifici e il rumore tecnico mediante un nuovo approccio per il raggruppamento di cellule, PRIMUS.

È emerso che nel corso della chemioterapia si verifica un significativo aumento dello stato cellulare associato allo stress, correlato a una scarsa sopravvivenza libera da progressione. Inoltre, hanno visto che la presenza di cellule tumorali in questo stato è correlata alla presenza di fibroblasti infiammatori associati al cancro. Quindi, la chemioterapia è associata alla risposta allo stress sia in cellule tumorali che stromali.

1. Stato dell'arte

Secondo i dati presenti in GLOBOCAN, nel 2020 circa il 3,40% dei cancri femminili è di tipo ovarico (313959 donne affette) e tale patologia ha provocato il 4,68% della mortalità femminile da cancro (207252 donne decedute). L'alta mortalità è spiegabile in quanto spesso la diagnosi è tardiva a causa della mancanza di strumenti di *screening* e della presenza di sintomi molto generali, che caratterizzano anche altre condizioni. Se l'OC viene identificato quando è già nello stadio metastatico, la probabilità di sopravvivenza a cinque anni dalla diagnosi è del 25%. Il tipo più comune di OC è il cancro ovarico epiteliale sieroso di alto grado (HGSOC), con una frequenza del 70-80%.

I pazienti con HGSOC metastatico generalmente seguono un percorso di cura che prevede una chemioterapia neoadiuvante (NACT) a base di platino e taxano, una chirurgia citoriduttiva di intervallo, una chemioterapia post-operatoria ed eventualmente una terapia di mantenimento con bevacizumab o con inibitori della poli (ADP-ribosio) polimerasi (PARP). Nonostante l'aggressività di questi trattamenti, nell'80% dei casi si verificano recidive. Come si vede in figura 1, le pazienti recidive possono essere classificate come "platino-sensibili" o "platino-resistenti" sulla base dell'intervallo senza platino (PFI). Queste ultime non potranno essere nuovamente sottoposte alla stessa chemioterapia. Potranno essere loro somministrate delle tipologie di farmaco limitate che, oltre a funzionare solo nel 10-35% delle pazienti e ad incrementare il rischio di una rapida progressione della malattia, devono essere adattate al singolo individuo per prevenire il peggioramento di effetti avversi preesistenti ed evitare ulteriori complicazioni.

Lo sviluppo di strategie per la cura dei HGSOC è complesso a causa della presenza di un'elevata eterogeneità intratumorale che cambia nel tempo, di poche mutazioni pilota che sono bersagliabili con farmaci e di un alto tasso di alterazioni del numero di copie in geni appartenenti a numerose vie di segnalazione.

L'assenza di farmaci efficaci implica un'elevata mortalità nelle pazienti resistenti. Per questo motivo, è importante superare la resistenza al platino.

Come si può vedere in figura 2, sono diversi i meccanismi molecolari coinvolti nella chemioresistenza, per cui non è semplice identificare biomarcatori che permettano di prevedere la risposta di ogni individuo alla terapia e possibili bersagli di nuove strategie terapeutiche. Per rispondere a queste necessità, Zhang *et al.* hanno caratterizzato l'espressione genica in pazienti affette da HGSOC al momento della diagnosi iniziale e dopo l'esposizione alla NACT.

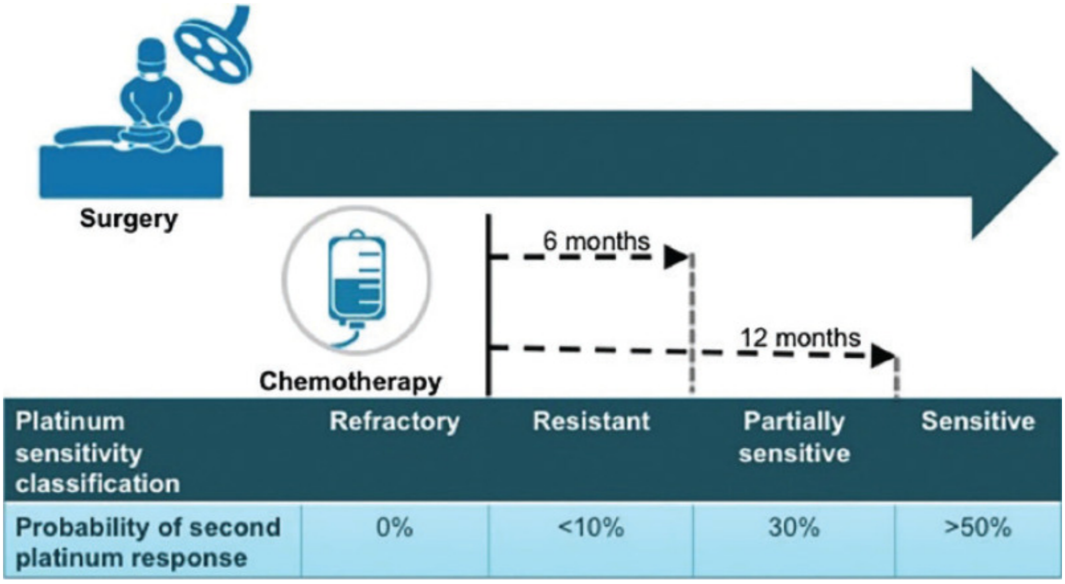

Platinum sensitivity classification	Refractory	Resistant	Partially sensitive	Sensitive
Probability of second platinum response	0%	<10%	30%	>50%

Figura 1: Definizione di platino-resistenza.
Fonte: A brief review of the management of platinum-resistant–platinum-refractory ovarian cancer

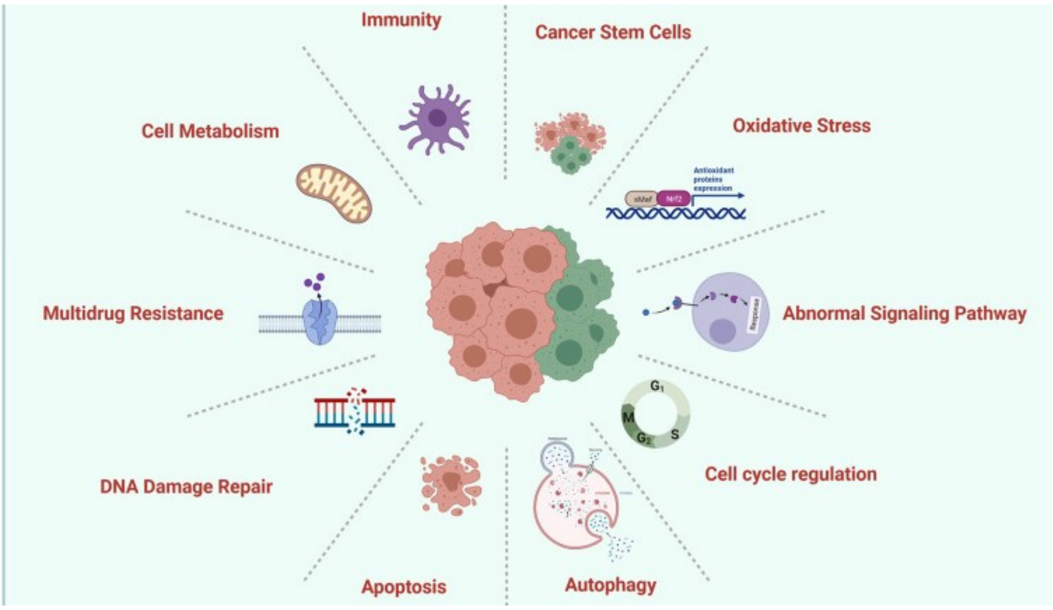

Figura 2: Meccanismi della resistenza alla chemioterapia a base di platino nel cancro ovarico.
Fonte: Molecular mechanisms of platinum-based chemotherapy resistance in ovarian cancer

Numerosi studi hanno usato i profili di espressione genica per predire la risposta alla chemioterapia a base di platino in donne con HGSOC metastatico basandosi su analisi longitudinali retrospettive. Infatti, dato che un approccio longitudinale consiste nell'effettuare misurazioni a tempi diversi, cioè permette di confrontare lo stato di un paziente prima e dopo un trattamento, esso è ideale per lo studio dei cambiamenti che avvengono durante la chemioterapia. Anche l'articolo di Zhang *et al.* si basa su un'analisi longitudinale, che però è di tipo prospettico. Gli studi retrospettivi iniziano dopo che il *follow-up* dei pazienti è stato concluso, mentre quelli prospettici prevedono la composizione di una coorte di pazienti che viene poi seguita nel tempo. La prima tipologia di studio menzionata è più veloce ed economica rispetto alla seconda, inoltre non è soggetta alla riduzione della numerosità e della rappresentatività del campione dovuta alla difficoltà nel seguire alcuni dei pazienti durante l'intera durata dello studio, ad esempio per l'eventuale decesso o per il cambio di ospedale. Tuttavia, risente di confondimento e di *bias* di selezione, e ha lo svantaggio di usare dati raccolti per scopi diversi da quello dei ricercatori (ad esempio per la cura del paziente).

Nell'articolo di Zhang *et al.* è stato utilizzato il *single cell RNA sequencing* (scRNA-seq) su campioni tissutali accoppiati isolati da 11 pazienti con HGSOC metastatico durante la laparoscopia diagnostica (campioni naïf al trattamento) e durante la chirurgia citoriduttiva (campioni post-NACT). È stata inferita la tipologia di ogni cellula in base al profilo di espressione. Applicando PRIMUS, un modello sviluppato dagli autori stessi, i dati sono stati normalizzati e le cellule tumorali sono state raggruppate in sottopopolazioni con profili trascrizionali simili. A questo punto sono stati identificati i geni differenzialmente espressi tra le varie sottopopolazioni e l'analisi di arricchimento di questi set di geni ha rivelato in quali *pathway* biologici sono coinvolti. Successivamente, per capire in quali delle sottopopolazioni ha effetto la chemioterapia, è stato fatto un confronto tra le proporzioni di ogni comunità cellulare in campioni accoppiati. Infine, è stata valutata la correlazione tra la chemioterapia e la struttura subclonale dei pazienti, è stato verificato se un profilo trascrizionale associato allo stress è predittivo di una scarsa risposta al trattamento, ed è stata studiata la relazione tra cellule tumorali e microambiente per identificare possibili bersagli di terapie per superare la chemioresistenza.

2. Approccio sperimentale

2.1 scRNA-seq

2.1.1 Introduzione

L'RNA svolge un ruolo fondamentale nella crescita e nel differenziamento cellulare, per questo una sua espressione anomala è associata alla comparsa, allo sviluppo, alla progressione e alla metastasi del tumore.

L'*RNA sequencing* (RNA-seq) è un approccio genomico che permette di analizzare le differenze di espressione genica e di definire diversi profili trascrittomici, i quali possono evidenziare le differenze tra diversi sottotipi, stadi di sviluppo o microambienti del tumore. Pertanto, è un potente strumento per comprendere i meccanismi molecolari dello sviluppo del cancro e sviluppare nuove strategie di prevenzione e trattamento.

Le firme trascrittomiche basate sul classico *bulk RNA-seq*, che usa come materiale di partenza il tessuto con tutte le popolazioni cellulari presenti, sono identificate a partire da dati di espressione genica media e raramente sono state usate nella pratica clinica a causa della bassa riproducibilità, determinata dai *bias* dovuti all'eterogeneità intra-tumorale.

I campioni di tessuto tumorale sono altamente eterogenei, sia perché oltre alle cellule tumorali contengono anche altri tipi di cellule come ad esempio quelle immunitarie e stromali, sia perché le cellule tumorali stesse sono uniche in quanto presentano diverse alterazioni somatiche, regolazioni trascrizionali e modificazioni epigenetiche. Per questo motivo, quando si ha a che fare con tessuti tumorali è conveniente usare il *single cell RNA sequencing* (scRNAseq) in modo da poter confrontare, oltre ai trascrittomi di campioni differenti, anche i trascrittomi di cellule dello stesso campione. Il scRNA-seq permette di studiare l'eterogeneità intra-popolazione e gli stati cellulari ad una risoluzione elevata, potenzialmente rivelando sottotipi cellulari o dinamiche di espressione genica che sono mascherate nelle misurazioni *bulk*.

2.1.2 Librerie per il scRNA-seq

Sono stati sviluppati molti protocolli per il scRNA-seq. Generalmente prevedono l'isolamento delle singole cellule dal tessuto, la lisi delle cellule preservando l'mR-

NA, la cattura dell'mRNA (tipicamente utilizzando dei poli(dT)), la retrotrasczione (in cui i primer per la trascrittasi inversa contengono sequenze UMI che marcano univocamente una molecola di mRNA) e l'amplificazione del cDNA che viene usato per la preparazione delle librerie per il sequenziamento.

Esistono dei kit commerciali e reagenti per svolgere tutti gli step di questi protocolli. In particolare, recentemente sono state sviluppate delle piattaforme microfluidiche in cui si fanno le reazioni di RNAseq in volumi dell'ordine di nanolitri, permettendo di risparmiare reagenti e di aumentare la sensitività della rilevazione e l'accuratezza quantitativa.

Il sistema Chromium di 10X Genomics permette di costruire una libreria in modo automatizzato usando un macchinario detto Chromium Connect, all'interno del quale si trova proprio una piattaforma microfluidica detta Chromium controller.

Nel Chromium controller un massimo di 10000 cellule vengono isolate ognuna in una goccia oleosa microscopica detta GEM. Le GEM restano separate l'una dall'altra perché sono emulsionate in un ambiente acquoso. In ogni GEM, oltre alla cellula, sono presenti una biglia contenente un codice a barre cellula-specifico (diverso in ogni biglia) e i reagenti per la retrotrascrizione. La biglia è coniugata con milioni di oligonucleotidi di 80 bp, in ognuno dei quali è presente un *primer* read 1 per il sequenziamento Illumina, un codice a barre cellula-specifico 10x (uguale in tutti gli oligonucleotidi coniugati alla stessa biglia), un *Unique Molecular Identifier* (UMI) e un poli(dT) per il legame all'mRNA.

In seguito alla lisi chimica delle cellule, gli mRNA di ogni singola cellula si legano agli oligonucleotidi della biglia corrispondente, avviene la retrotrascrizione e si originano dei cDNA che presentano lo stesso codice a barre. A questo punto, l'olio che forma le GEM viene rimosso portando al mescolamento di tutti i cDNA, che verranno in seguito sequenziati.

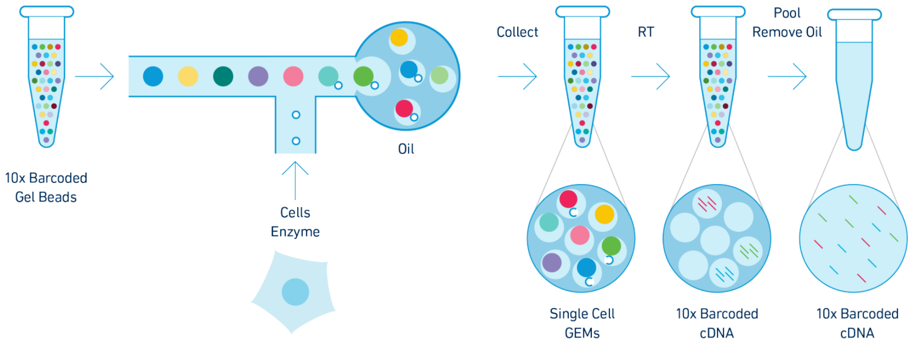

Figura 3a: Generazione delle GEM.
Fonte: 10X Genomics, Chromium - Single Cell 3' Reagent Kits v2 - User Guide.

Le librerie finali contengono anche i *primer* P5 e P7 per la bridge PCR Illumina, un *primer* read 2 per il sequenziamento Illumina e un indice del campione i7.

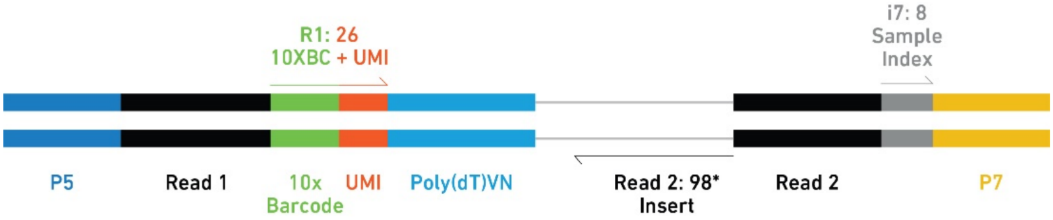

Figura 3b: Struttura finale della libreria Single Cell 3'.
Fonte: 10X Genomics, Chromium - Single Cell 3' Reagent Kits v2 - User Guide.

Oltre al Chromium System, vi sono altri metodi molto usati per il scRNA-seq, quali Fluidigm C1, SMART-seq2 e MARS-seq. Essi differiscono in termini di procedimento, sensitività, qualità dei dati e costo.

Analizzando le caratteristiche di queste piattaforme, riassunte nella figura 2, si giustifica la scelta di Zhang *et al.* di preparare le librerie di scRNA-seq con il kit Chromium.

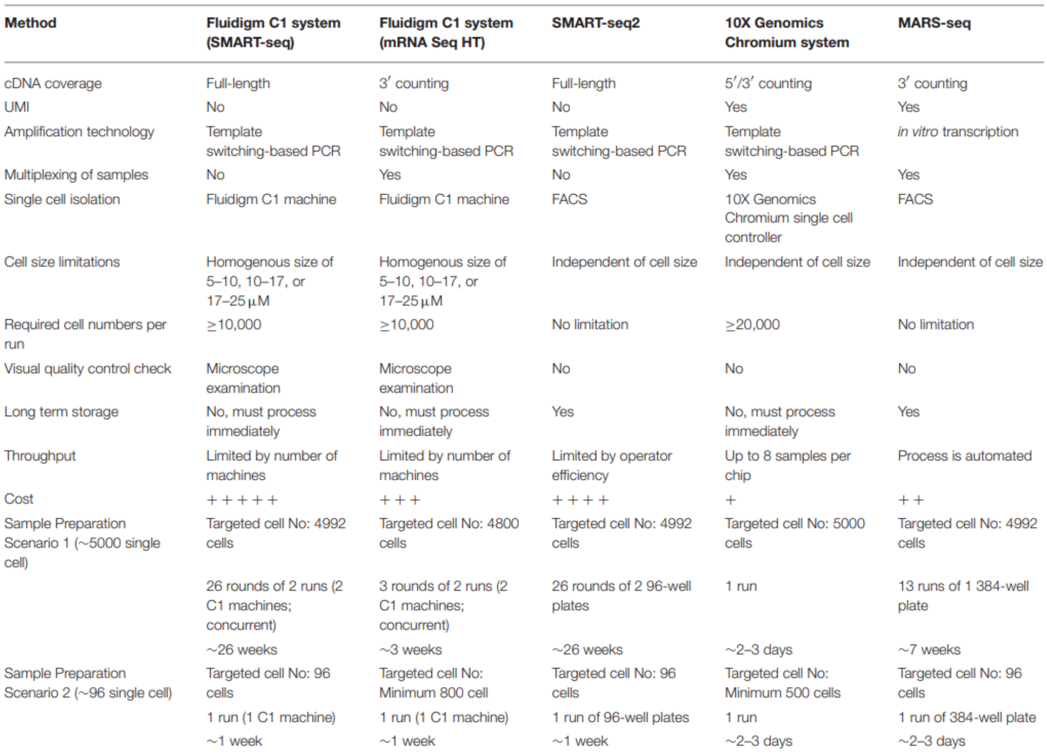

Method	Fluidigm C1 system (SMART-seq)	Fluidigm C1 system (mRNA Seq HT)	SMART-seq2	10X Genomics Chromium system	MARS-seq
cDNA coverage	Full-length	3′ counting	Full-length	5′/3′ counting	3′ counting
UMI	No	No	No	Yes	Yes
Amplification technology	Template switching-based PCR	Template switching-based PCR	Template switching-based PCR	Template switching-based PCR	*in vitro* transcription
Multiplexing of samples	No	Yes	No	Yes	Yes
Single cell isolation	Fluidigm C1 machine	Fluidigm C1 machine	FACS	10X Genomics Chromium single cell controller	FACS
Cell size limitations	Homogenous size of 5–10, 10–17, or 17–25 µM	Homogenous size of 5–10, 10–17, or 17–25 µM	Independent of cell size	Independent of cell size	Independent of cell size
Required cell numbers per run	≥10,000	≥10,000	No limitation	≥20,000	No limitation
Visual quality control check	Microscope examination	Microscope examination	No	No	No
Long term storage	No, must process immediately	No, must process immediately	Yes	No, must process immediately	Yes
Throughput	Limited by number of machines	Limited by number of machines	Limited by operator efficiency	Up to 8 samples per chip	Process is automated
Cost	+ + + + +	+ + +	+ + + +	+	+ +
Sample Preparation Scenario 1 (~5000 single cell)	Targeted cell No: 4992 cells	Targeted cell No: 4800 cells	Targeted cell No: 4992 cells	Targeted cell No: 5000 cells	Targeted cell No: 4992 cells
	26 rounds of 2 runs (2 C1 machines; concurrent)	3 rounds of 2 runs (2 C1 machines; concurrent)	26 rounds of 2 96-well plates	1 run	13 runs of 1 384-well plate
	~26 weeks	~3 weeks	~26 weeks	~2–3 days	~7 weeks
Sample Preparation Scenario 2 (~96 single cell)	Targeted cell No: 96 cells	Targeted cell No: Minimum 800 cell	Targeted cell No: 96 cells	Targeted cell No: Minimum 500 cells	Targeted cell No: 96 cells
	1 run (1 C1 machine)	1 run (1 C1 machine)	1 run of 96-well plates	1 run	1 run of 384-well plate
	~1 week	~1 week	~1 week	~2–3 days	~2–3 days

Figura 4a: Caratteristiche dei metodi per generare librerie per il scRNA-seq.
Fonte: A Single-Cell Sequencing Guide for Immunologists

Con il Chromium System e con il MARS-seq, che sono metodi basati sull'etichetta molecolare, è possibile processare i campioni in un'unica provetta per la generazione della libreria e quindi il processo costa meno e aumenta il rendimento (possono essere analizzate molte cellule). Inoltre, grazie all'inserimento delle sequenze UMI prima dell'amplificazione, i livelli di espressione di singoli geni in singole cellule possono essere quantificati digitalmente riducendo la variabilità tecnica e i bias introdotti durante la PCR. Un lato negativo è che la sensitività (cioè il numero minimo di molecole di un tipo di mRNA richiesto per la sua rilevazione) è minore rispetto ai metodi *full-length*, come Fluidigm C1 e SMART-Seq2, perché le *reads* sono ristrette a una sola estremità del trascritto. Dato che un'alta sensitività è importante per permettere la rilevazione di geni debolmente espressi, in studi di livelli d'espressione genica e di composizione tissutale non è così essenziale e quindi è preferibile usare metodi basati sull'etichetta molecolare per poter analizzare più cellule.

La differenza principale tra il Chromium System e il MARS-seq è che il primo è un sistema *droplet-based* mentre il secondo *plate-based.* Zhang *et al.* hanno misurato il trascrittoma di 93650 cellule provenienti da 22 campioni. Dato che nella piattaforma del MARS-seq possono essere processate 384 cellule alla volta impiegando 2/3 giorni, non sarebbe stato funzionale usare questo metodo, in quanto ci sarebbero voluti più di 2 anni per concludere la procedura. Con il Chromium System, invece, è possibile processare contemporaneamente fino a 10000 cellule per ognuno degli 8 campioni contenibili nel chip in 2/3 giorni. Con questo metodo sono quindi sufficienti meno di due settimane.

2.1.3 Sequenziamento Illumina

Le piattaforme per il sequenziamento supportate per le librerie 3' *single cell* sono Illumina MiSeq, NextSeq 500/550, HiSeq 2500, HiSeq 3000/4000 e NovaSeq. Secondo quanto scritto in “An introduction to Next-Generation Sequencing Technology” e “Single-Cell Sequencing Workflow: Critical Steps and Considerations” di Illumina:

- MiSeq è poco indicata per il sequenziamento del trascrittoma;
- NextSeq 500 è obsoleta;
- NextSeq 550 è ideale per sequenziamenti *single cell* su piccola scala;
- HiSeq 2500, 3000 e 4000 sono diventate obsolete nel corso del 2022, HiSeq 2000 ha una *flow cell single-read* mentre HiSeq 3000 e 4000 hanno una *flow cell paired-end*, la principale differenza tra HiSeq 3000 e 4000 è che la seconda è più produttiva;

- NovaSeq 6000 è la piattaforma più produttiva e affidabile per sequenziamenti *single cell* su grande scala.

La scelta di Zhang *et al.*, che hanno effettuato il sequenziamento con HiSeq 2500, HiSeq 4000 e NovaSeq 6000 prima che le piattaforme HiSeq diventassero obslete, è quindi giustificata.

Tutte le piattaforme Illumina, prima di procedere con il sequenziamento, prevedono l'amplificazione delle librerie tramite bridge PCR. Questa reazione avviene in apposite *flow cell.* I cDNA delle librerie presentano alle due estremità sequenze P5 e P7 che sono complementari agli oligonucleotidi P5 e P7 di cui è ricoperta la superficie della *flow cell.* Quindi un cDNA si ibriderà prima con un oligonucleotide complementare a una delle sue due estremità e poi anche a un oligonucleotide complementare all'altra estremità, formando un ponte. In seguito a cicli di denaturazione ed estensione, intorno al punto della *flow cell* in cui si era ibridato un cDNA si forma un *cluster* di cloni di quella molecola.

Le molecole che compongono i vari *cluster* vengono rese a singolo filamento e si può procedere con il sequenziamento Illumina, che avviene nei seguenti step:

1. Nella *flow cell* vengono aggiunti dei reagenti tra cui dei *primer*, complementari a read 1 e read 2, e dei terminatori reversibili, ovvero nucleotidi che presentano il gruppo 3'-OH bloccato e che sono coniugati a un fluoroforo nucleotide-specifico.
2. I *primer*, che si ibridano a read 1 e read 2, vengono estesi dalla polimerasi, che incorpora il terminatore reversibile complementare alla prima base.
3. Dopo aver rimosso i terminatori reversibili che non hanno reagito, si rileva la fluorescenza di ogni cluster per capire quale base è stata incorporata.
4. Il blocco all'estremità 3'-OH del terminatore reversibile viene rimosso grazie a un apposito agente riducente e viene catalizzata l'eliminazione del fluoroforo.
5. Vengono aggiunti nuovamente i reagenti per procedere con un altro ciclo di sequenziamento identico al primo.

L'analisi sequenziale di cicli multipli di sequenziamento permette di risalire alla sequenza nucleotidica di ogni frammento di templato, che viene restituita sotto forma di file FASTQ.

Nella stessa *flow cell* possono essere sequenziate più librerie simultaneamente grazie alla presenza del codice a barre 10x e dell'indice di campione i7, che permettono di poter risalire a quale libreria appartiene la molecola sequenziata.

2.2 Analisi di dati scRNA-seq

2.2.1 Preprocessamento di dati scRNA-seq

Il preprocessamento di dati di scRNA-seq che derivano da librerie costruite con sistemi *droplet-based*, come Chromium di 10x Genomic, è dato dal susseguirsi di vari passaggi.

1. Nel primo passaggio, detto *demultiplexing*, nelle sequenze grezze in formato FASTQ vengono individuati i codici a barre cellulari e gli UMI, che vengono aggiunti all'intestazione della conta.
2. Nel secondo passaggio, le *reads* vengono allineate a un genoma o a un trascrittoma di riferimento.
3. Nel terzo passaggio, gli UMI vengono collassati per eliminare le molecole duplicate per PCR dalle *reads* in ogni cellula, superando quindi i *bias* quantitativi dovuti all'amplificazione.
4. Nel quarto passaggio, le *reads* vengono divise in base al codice cellula-specifico e viene costruita una matrice di conte con le cellule nelle colonne e i geni nelle righe.
5. Nel quinto passaggio, le cellule di bassa qualità e i geni con bassa abbondanza vengono eliminati dalla matrice.

I software più utilizzati per svolgere questi passaggi sono alevin-fry, salmon alevin, Cell Ranger, dropSeqpipe, kallisto bustools, Optimus, scPipe e zUMIs. You Y *et al.*, nell'articolo "Benchmarking UMI-based single-cell RNA-seq preprocessing workflows", li hanno comparati e hanno visto differenze significative riguardanti la quantità di memoria utilizzata, il tempo di esecuzione, l'uso della CPU e la scalabilità. Come si vede nei grafici della figura 3a, zUMI e dropSeqPipe sono quelli che impiegano più memoria e tempo, salmon alevin e alevin-fry sono quelli che impiegano più CPU, e Cell Ranger e dropSeqPipe sono quelli con una scalabilità migliore in quanto saturano passando da 16 a 32 thread. Inoltre, dalla figura 3b, Cell Ranger e salmon alevin rilevano molti più geni con alti picchi di conte per gene rispetto agli altri software.

Queste considerazioni spiegano la scelta di Zhang *et al.* di usare Cell Ranger, che oltretutto è stato sviluppato per essere usato con la piattaforma Chromium.

Le *reads* sono state allineate sul genoma GRCh38.d1.vd1 e i geni sono stati mappati secondo l'annotazione genica GENCODE v25.

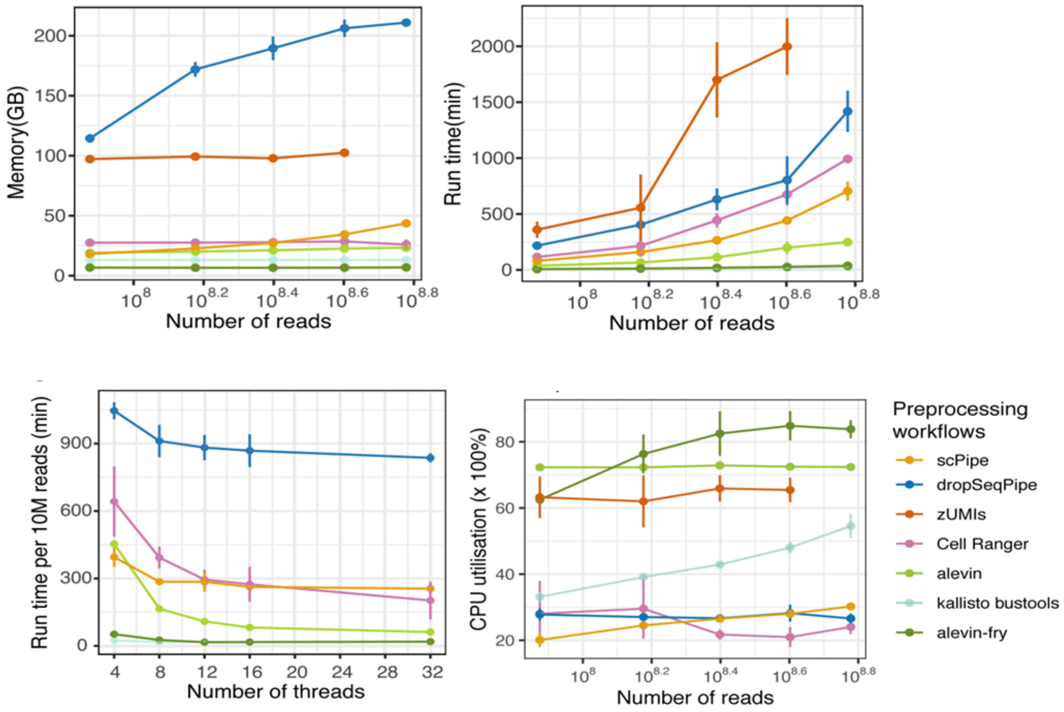

Figura 5a: Performance dei diversi software di preprocessamento di dati di scRNA-seq
Fonte: Benchmarking UMI-based single-cell RNA-seq preprocessing workflows

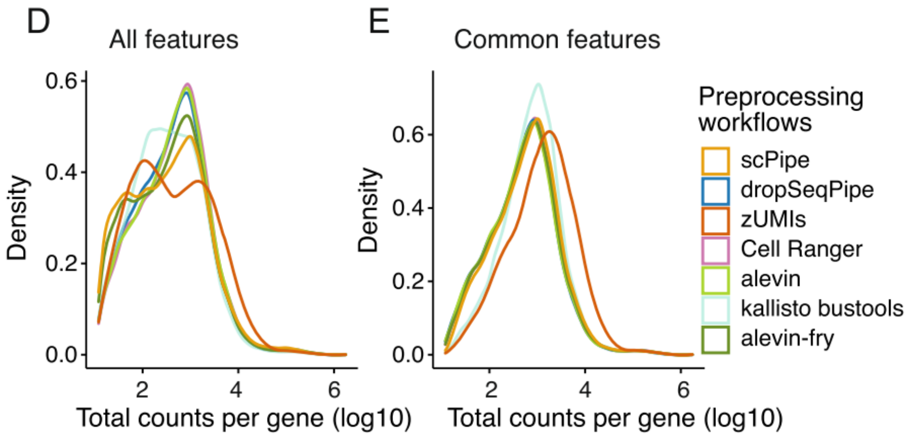

Figura 5b: Densità di conte per gene
Fonte: Benchmarking UMI-based single-cell RNA-seq preprocessing workflows

Le cellula a bassa qualità sono state eliminate attraverso tre filtraggi sequenziali. Prima sono state escluse le cellule esprimenti combinazioni di PAX8, DCN e PTPRC per rimuovere potenziali doppioni e le cellule con più di un 15% di conte UMI originate da geni mitocondriali. Poi, usando il pacchetto di R Seurat v3, è stato effettuato un iniziale *clustering* delle cellule e, sulla base della distribuzione bimodale dei tipi cellulari (epiteliale, stromale e immunitario), sono stati stabiliti quali valori di numero di *reads*, numero di conte UMI, numero di geni e percentuale di conte UMI generate da geni mitocondriali dovevano essere rispettati dalle cellule. Infine, sono state filtrate le cellule epiteliali con profili *copy number alteration* (CNA) che venivano raggruppate con le cellule stromali.

2.2.2 Normalizzazione e clustering di dati di scRNA-seq

L'eterogeneità dei dati di scRNA-seq non è determinata soltanto dalla variazione biologica tra i diversi tipi e stati cellulari, ma anche da errori tecnici introdotti durante l'elaborazione sperimentale. Ad esempio, la profondità di sequenziamento è variabile tra campioni. Anche l'efficienza di cattura dell'mRNA e della retrotrascrittasi è variabile e causa una differenza nelle conte UMI delle cellule anche se il numero di molecole nelle cellule è identico. Inoltre, soprattutto se i dati derivano da tecnologie *droplet-based*, sono presenti molti *dropout*, ovvero conte con valori pari a zero. Quest'ultimo fenomeno può essere dovuto sia a una bassa quantità di mRNA nella cellula, sia a una sua inefficiente cattura, sia alla stocasticità della sua espressione. La conseguenza del *dropout* è che i dati sono molto sparsi e presentano un eccesso di zeri, per cui catturano sono una piccola frazione del trascrittoma di ogni cellula.

Per questo motivo, dopo aver filtrato i dati di bassa qualità, è necessario procedere con la normalizzazione, che serve per aggiustare i *bias* cellula-specifici, in modo che non vengano mascherate le differenze biologiche.

L'alta frequenza dei *dropout* interferisce con le classiche normalizzazioni che vengono effettuate per dati di *bulk* RNA-seq. Si potrebbe procedere rimuovendo in ogni cellula i geni con conte pari a 0, ma questo potrebbe introdurre dei *bias* in quando i geni con conte pari a 0 variano a seconda della cellula. Quindi, sono stati sviluppati dei metodi che normalizzano i dati facendoli aderire a delle distribuzioni parametriche quali la Poisson, la binomiale negativa e meno frequentemente la binomiale negativa zero-inflated, che è ridondante nel caso in cui siano presenti le conte UMI.

Dopo la normalizzazione, solitamente si usa una tecnica statistica per la riduzione della dimensione, in modo da sintetizzare i dati del dataset minimizzando la perdita d'informazione. La più comune per i dati di *bulk* RNA-seq è l'analisi delle componenti principali (PCA). Infine, viene applicato un algoritmo che raggruppa le cellule simili, le quali sono vicine nel grafico PCA. La PCA, però, basandosi sulla geometria euclidea, non è appropriata per dati molto sparsi, discreti e distorti come quelli di scRNA-seq.

Zhang *et al.* hanno sviluppato un modello, detto PRIMUS (Poisson scRNA integration of mixed unknown signals) che normalizza i dati di scRNA-seq e raggruppa le cellule sulla base della somiglianza dei loro profili trascrizionali. Il profilo trascrizionale di ogni cellula viene approssimato da una distribuzione di Poisson:

$$Y_{j,i} \sim Poisson\left(\left(\sum_{l=1}^{r}\left(X_{j,l}D_{l,i}\right)\right)+\left(\sum_{c=1}^{k}\left(Z_{j,c}C_{c,i}\right)\right)G_i\right) \tag{1}$$

dove $Y_{i,j}$ indica le conte UMI del gene j nella cellula i-esima, $X_{j,l}$ indica il centroide del profilo d'espressione del gene j con fattore di rumore l, $D_{l,i}$ indica il coefficiente di disegno dell'l-esimo fattore di rumore nella i-esima cellula, $Z_{j,c}$ indica il centroide del profilo di espressione del cluster c per il gene j, $C_{c,i}$ può avere valore 0 o 1 e indica se la cellula i-esima appartiene al *cluster* c, e G_j è un fattore di ridimensionamento cellula-specifico.

Dati $Y_{j,i}$, $D_{l,i}$, G_i e il numero di *cluster k*, che viene posto uguale a 12 sulla base del criterio di informazione Bayesiano (BIC), usando un algoritmo di aspettazione-massimizzazione (EM) si possono stimare $X_{j,l}$, $Z_{j,c}$ e $C_{c,i}$. Il parametro θ = ($X_{j,l}$, $Z_{j,c}$, $C_{c,i}$) viene stimato iterando una fase di aspettazione e una di massimizzazione fino ad arrivare a convergenza. Nella fase di aspettazione vengono stimati $X_{j,l}$ e $Z_{j,c}$ dati $Y_{j,i}$, $D_{l,i}$, $C_{c,i}$, e G_i. Nella fase di massimizzazione viene aggiornato $C_{c,i}$ dati $Y_{j,i}$, $D_{l,i}$, G_i e i parametri stimati nel passaggio di aspettazione $X_{j,l}$ e $Z_{j,c}$. Infine, dati $Y_{j,i}$, $D_{l,i}$, G_i e θ, viene calcolata $\widetilde{Z}_{j,i}$, ovvero l'espressione del gene j nella cellula i una volta eliminato il rumore, considerando:

$$Y_{j,i} \sim Poisson\left(\left(\sum_{l=1}^{r}\left(X_{j,l}D_{l,i}\right)\right)+\widetilde{Z}_{j,i}\right)G_i) \tag{2}$$

PRIMUS è un modello lineare, che tiene conto dell'additività dei segnali biologici e del rumore tecnico, e stocastico, che tiene conto dell'esistenza di una naturale variazione tra le cellule. Inoltre, è adatto a trattare dati con molti *dropout*. Rispetto ad altri metodi di integrazione di dati di scRNA-seq quali Seurat v3, Harmony, LIGER, mnnCorrect e fastMNN, e di dati di bulk RNA-seq quali ComBat, ComBat-seq e limma, Zhang *et al.* hanno dimostrato che PRIMUS clusterizza le cellule accuratamente anche in caso di composizioni cellulari eterogenee e di un numero sbilanciato di cellule in diverse fonti. Queste caratteristiche lo rendono ideale per essere usato su dati di sc-RNAseq di campioni tumorali.

2.2.3 Identificazione e analisi funzionale dei geni differenzialmente espressi

Una volta che le cellule tumorali sono state divise in gruppi con PRIMUS, si devono identificare i geni differenzialmente espressi tra i vari *cluster* di cellule.

Zhang *et al.* hanno effettuato un test del rapporto di verosimiglianza (LTR) per ogni coppia di *cluster*, quindi $C_{12,2} = \binom{12}{2} = \frac{12!}{(12-2)!2!} = 66$ test. Poi hanno creato una lista di geni differenzialmente espressi tenendo in considerazione i 1000 più significativi rilevati in ogni test. Usando l'algoritmo di Walktrap, hanno identificato delle comunità di geni differenzialmente espressi. Dopo aver effettuato una serie di filtraggi per restringere il numero di comunità e il numero di geni in ognuna di esse, hanno valutato la presenza di una sovra-rappresentazione di alcune firme geniche in ogni comunità mediante un'analisi di *gene set* e le hanno associate a dei processi biologici mediante un'analisi dei *pathway*.

Successivamente, per capire se la chemioterapia ha effetto su cellule con una determinata firma genica, Zhang *et al.* hanno valutato la presenza di una differenza significativa nella percentuale di cellule appartenenti ai *cluster* cellulari caratterizzati da quella firma in campioni pre e post-trattamento.

2.3 Inferenza della struttura subclonale

Per capire se l'aumento della percentuale di cellule nello stato associato allo stress durante la chemioterapia sia dovuto alla loro induzione e/o alla loro maggior capacità di sopravvivenza rispetto alle cellule negli altri stati, Zhang *et al.* hanno valutato l'espansione e la capacità proliferativa dei subcloni ad alto e basso stato di stress durante la chemioterapia.

Hanno usato il pacchetto di R "infercnv" per identificare le alterazioni del numero di copie (CNA) a partire dai dati di scRNA-seq e hanno usato i profili CNA per inferire la struttura subclonale di ogni paziente. Questo pacchetto permette di comparare l'intensità dell'espressione genica lungo le posizioni del genoma con quella di un set di cellule di riferimento e di generare una *heatmap* che rende immediatamente evidente quali regioni del genoma sono più o meno abbondanti del normale. Zhang *et al.*, come set di cellule di riferimento hanno usato 150 cellule stromali di ogni paziente campionate in modo casuale.

2.4 Metodi per lo studio dell'interazione tra cellule tumorali e stromali

Zhang *et al.* hanno studiato la relazione tra la presenza di cellule tumorali nello stato associato allo stress e la composizione del microambiente tumorale.

Per clusterizzare le cellule stromali è stato usato il pacchetto R "Seurat v3". Dato che l'espressione della maggior parte dei geni non è significativamente variabile tra le cellule, a partire dai dati di scRNA-seq sono stati identificati i primi 3000 geni altamente variabili (HVG) tra le cellule, ovvero gli outlier nel grafico media-varianza, usando la funzione "FindVariableFeatures" con metodo "vst". Poi l'espressione dei 3000 HVG è stata centrata e normalizzata con la funzione "ScaleData". Infine, su questi dati è stata effettuata una PCA e le prime 50 componenti sono state usate per identificare i *cluster* di cellule usando un algoritmo SNN basato sull'ottimizzazione della modularità. Il tipo delle cellule appartenenti ai vari *cluster* è poi stato predetto usando il software Scibet.

Per capire in che stato è ogni cellula è stata fatta una analisi della traiettoria usando il pacchetto R "Monocle" v3. Questo software usa un algoritmo per inferire la sequenza dei cambiamenti nell'espressione genica che si verificano nelle cellule durante il corso dei processi biologici e per capire in quale punto di questa traiettoria è la cellula. Prima i dati sono stati preprocessati usando PRIMUS, poi sono state usate diverse funzioni di Monocle 3 per: ridurre la dimensionalità dei dati con l'algoritmo UMAP (reduce_dimension), raggruppare le cellule a seconda della traiettoria a cui appartengono (cluster_cells) e creare un grafico in cui ogni cellula viene visualizzata nell'esatta posizione della sua traiettoria (learn_graph).

Per identificare i marcatori dei vari sottotipi di fibroblasti associati al cancro (CAF) e i geni differenzialmente espressi tra campioni di cellule ad alto e basso stress presenti nel microambiente tumorale, è stata usata la funzione "FindMarkers" del pacchetto R "Seurat" v3.

Per studiare le interazioni tra le cellule tumorali nello stato ad alto stress e i CAF di tipo infiammatorio presenti nel microambiente tumorale è stato usato il pacchetto R "nichenetr", che combina i dati di espressione genica di queste cellule con conoscenze pregresse sulle vie di segnalazione e regolazione genica per predire le interazioni ligando-recettore, che potrebbero portare a cambiamenti di espressione genica nelle cellule che interagiscono. Quindi, nichenetr identifica i ligandi che influenzano l'espressione in un'altra cellula, i geni influenzati da ogni ligando e i mediatori coinvolti nelle vie di trasduzione del segnale che vengono attivate.

3. Risultati e discussione

3.1 Identificazione di firme geniche nei sottotipi di cellule tumorali

Hanno superato il controllo di qualità 51786 cellule delle 93650 su cui Zhang *et al.* hanno eseguito il scRNA-seq. Di queste cellule, 8806 sono state classificate come epiteliali tumorali, 8045 come stromali e 34935 come immunitarie.

Mediante PRIMUS, le cellule epiteliali tumorali sono state divise in 12 *cluster* e, in seguito all'analisi dei geni differenzialmente espressi tra di essi, sono state identificate 10 firme genetiche. Queste sono poi state associate a dei percorsi biologici tramite l'analisi dei *pathway*. I *cluster* C1, C2, C6 e C12, non avendo firme genetiche sovrarappresentate, non sono stati considerati nelle analisi successive. Le firme genetiche, i *pathway* e i geni di ogni firma che possono essere usati come marcatori sono riportati in figura 6.

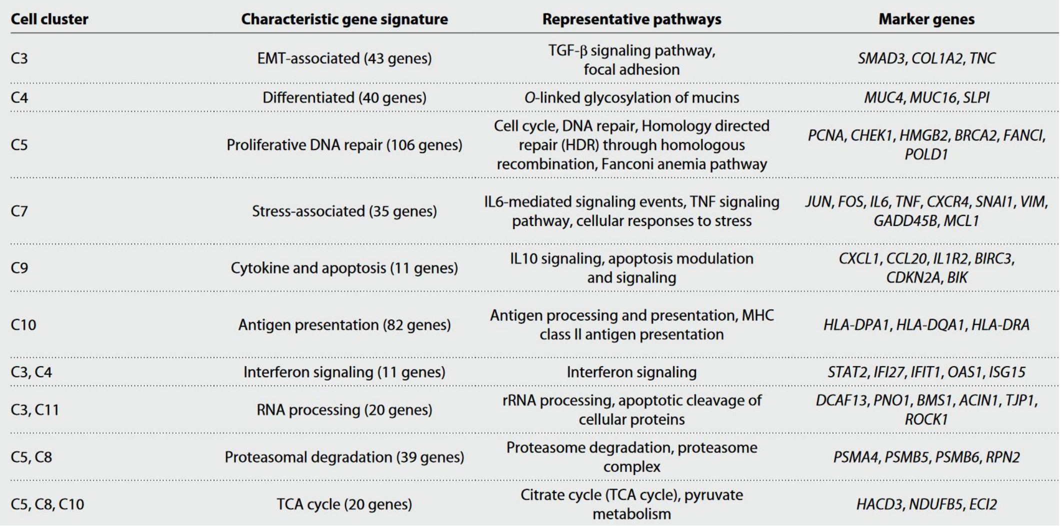

Cell cluster	Characteristic gene signature	Representative pathways	Marker genes
C3	EMT-associated (43 genes)	TGF-β signaling pathway, focal adhesion	*SMAD3, COL1A2, TNC*
C4	Differentiated (40 genes)	*O*-linked glycosylation of mucins	*MUC4, MUC16, SLPI*
C5	Proliferative DNA repair (106 genes)	Cell cycle, DNA repair, Homology directed repair (HDR) through homologous recombination, Fanconi anemia pathway	*PCNA, CHEK1, HMGB2, BRCA2, FANCI, POLD1*
C7	Stress-associated (35 genes)	IL6-mediated signaling events, TNF signaling pathway, cellular responses to stress	*JUN, FOS, IL6, TNF, CXCR4, SNAI1, VIM, GADD45B, MCL1*
C9	Cytokine and apoptosis (11 genes)	IL10 signaling, apoptosis modulation and signaling	*CXCL1, CCL20, IL1R2, BIRC3, CDKN2A, BIK*
C10	Antigen presentation (82 genes)	Antigen processing and presentation, MHC class II antigen presentation	*HLA-DPA1, HLA-DQA1, HLA-DRA*
C3, C4	Interferon signaling (11 genes)	Interferon signaling	*STAT2, IFI27, IFIT1, OAS1, ISG15*
C3, C11	RNA processing (20 genes)	rRNA processing, apoptotic cleavage of cellular proteins	*DCAF13, PNO1, BMS1, ACIN1, TJP1, ROCK1*
C5, C8	Proteasomal degradation (39 genes)	Proteasome degradation, proteasome complex	*PSMA4, PSMB5, PSMB6, RPN2*
C5, C8, C10	TCA cycle (20 genes)	Citrate cycle (TCA cycle), pyruvate metabolism	*HACD3, NDUFB5, ECI2*

Figura 6: Firme genetiche, *pathway* e marcatori di ogni *cluster*
Fonte: Longitudinal single-cell RNA-seq analysis reveals stress-promoted chemoresistance in metastatic ovarian cancer

3.2 Correlazione tra chemioterapia e cellule tumorali di sottotipo associato allo stress

Dal confronto tra le proporzioni dei *cluster* di cellule tumorali presenti in più pazienti (C4, C5, C7, C8 e C11) in campioni naïf al trattamento e post-NACT è emerso che mediamente durante la chemioterapia c'è una variazione significativa nelle percentuali di cellule di C5 (firma *proliferative DNA repair*), che diminuiscono dal 14% al 3%, e C7 (firma associata allo stress), che aumentano dal 3% al 17%.

La firma *proliferative DNA repair* presenta geni coinvolti nel ciclo cellulare, nella riparazione del DNA, nella ricombinazione omologa e nella riparazione dei legami incrociati interfilamento del DNA.

La firma associata allo stress presenta geni coinvolti nella via di segnalazione mediata dall'interleuchina 6 (IL6), nella via di segnalazione mediata dal fattore di necrosi tumorale e in processi che causano il cambiamento dello stato o dell'attività di una cellula come risultato di uno stimolo stressante.

La riduzione di C5 potrebbe essere dovuta o alla morte della maggior parte delle cellule proliferative o all'arresto del ciclo cellulare. L'aumento di C7, invece, potrebbe essere dovuto o all'induzione dello stato cellulare associato allo stress e/o alla maggior propensione alla sopravvivenza delle cellule in questo stato.

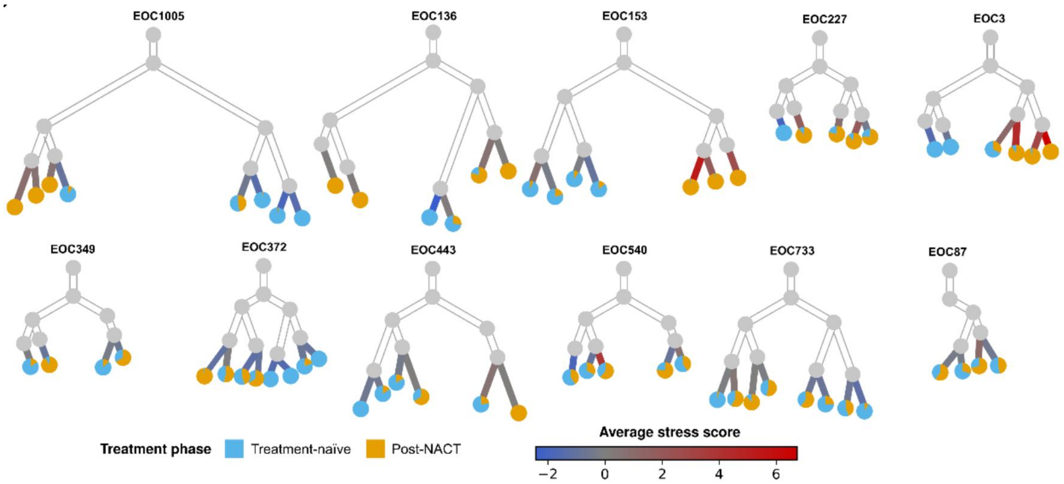

Figura 7: Strutture subclonali degli 11 pazienti. Ogni subclone è rappresentato da un nodo, raffigurato come un diagramma a torta in cui l'ampiezza delle fette azzurra e gialla è rispettivamente proporzionale alla percentuale del subclone nei campioni naïf al trattamento e nei campioni post-NACT. La gradazione di colore di ogni ramo indica il punteggio di stress del subclone corrispondente.
Fonte: Longitudinal single-cell RNA-seq analysis reveals stress-promoted chemoresistance in metastatic ovarian cancer - Supplementary Materials

L’analisi delle strutture subclonali degli 11 pazienti (figura 7), inferite dai dati di scRNA-seq, ha confermato che durante la chemioterapia aumentano le cellule nello stato associato allo stress, in quanto in tutti i pazienti si può notare una maggiore estensione dei subcloni con alto punteggio di stress rispetto agli altri. Inoltre, quest’analisi ha evidenziato che il grado di proliferazione dei subcloni a basso stress diminuisce nel corso del trattamento, mentre quello dei subcloni ad alto stress rimane costante. Quest’osservazione implica che l’aumento di C7 sia dovuto alla maggior propensione alla proliferazione di queste cellule rispetto a quelle con un profilo trascrizionale a basso stress. Quindi, la resistenza alla chemioterapia è correlata agli stati cellulari preesistenti e indotti.

Lo studio di Zhang *et al.* è il primo ad aver dimostrato che in un tumore umano, nel corso della chemioterapia, si verifica un aumento nella percentuale di cellule in un determinato stato trascrizionale.

Per confermare l’ipotesi che siano i profili trascrizionali delle cellule tumorali prima del trattamento a influenzare lo sviluppo della resistenza, Zhang *et al.* hanno utilizzato dati clinici e di *bulk* RNA-seq di 271 pazienti presenti in *The Cancer Genome Atlas* (TCGA). Dopo aver etichettato questi pazienti in base al loro punteggio di stress alla diagnosi ed aver effettuato un’analisi di sopravvivenza con il metodo di Kaplan-Meier, sono giunti alla conclusione che i pazienti ad alto punteggio di stress hanno una sopravvivenza libera da progressione (PFS) significativamente più corta di quelli a basso punteggio di stress (figura 8): il valore mediano di PFS nel primo gruppo di pazienti è di 14,9 mesi e nei secondi è di 21,2 mesi.

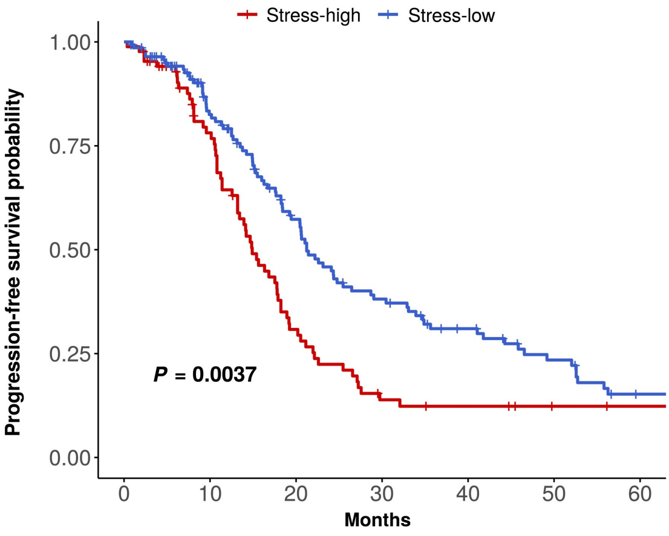

Figura 8: PFS dei pazienti della coorte del TCGA ad alto e basso stress.
Fonte: Longitudinal single-cell RNA-seq analysis reveals stress-promoted chemoresistance in metastatic ovarian cancer

Quindi, la presenza di un profilo trascrizionale correlato allo stress in tumori naïf al trattamento è un predittore della scarsa risposta alla chemioterapia.

3.3 Correlazione tra cellule tumorali ad alto stress e composizione del microambiente tumorale

Nei campioni tumorali, Zhang *et al.* hanno identificato 10 tipi di cellule immunitarie: cellule B, due tipi di cellule dendritiche, cellule linfoidi innate, macrofagi, mastociti, cellule natural killer, cellule dendritiche plasmacitoidi, plasmacellule e cellule T. Ognuna di queste tipologie cellulari è presente approssimativamente in uguale proporzione in campioni tumorali ad alto stress e a basso stress, però sono state evidenziate alcune differenze nella proporzione di cellule in un determinato stato trascrizionale. Rispetto ai campioni a basso stress, in quelli ad alto stress sono presenti meno cellule T CD8+ effettrici della memoria (fondamentali per la risposta immunitaria anti-tumorale), più precursori di cellule T CD8+ esaurite (non efficaci nell'eliminazione delle cellule tumorali, in quanto presentano una sovraespressione dei recettori inibitori e una diminuzione della produzione di citochine) e più macrofagi con funzione immunosoppressiva (hanno un elevata espressione di geni che inibiscono la reazione immunitaria, ad esempio TREM2, il quale è associato all'esaurimento delle cellule T).

Quindi, anche se lo stato trascrizionale delle cellule tumorali non è collegato alla prevalenza del tipo di cellule immunitarie, esso influenza lo stato trascrizionale delle cellule immunitarie: cellule tumorali ad alto stress sono correlate a una compromissione del sistema immunitario.

Nei campioni tumorali, Zhang *et al.* hanno identificato anche 5 tipi di cellule stromali, ovvero cellule endoteliali, cellule mesenchimali e tre sottopopolazioni di fibroblasti associati al cancro (CAF): CAF-1, CAF infiammatori (iCAF) e CAF-3.

Di queste tipologie cellulari, solo gli iCAF sono significativamente più abbondanti in campioni ad alto stress.

Come si vede in figura 9, l'analisi delle interazioni ricettore-ligando tra le cellule tumorali nello stato ad alto stress e gli iCAF rivela l'esistenza di un ciclo paracrino di tipo *feed-forward*: quando TNF e IL6 prodotti dalle cellule tumorali ad alto stress interagiscono con i loro recettori espressi dai CAF ne inducono il fenotipo iCAF, a loro volta gli iCAF producono ligandi (inclusi IL6 e TNF) che vengono riconosciuti dalle cellule tumorali nelle quali inducono la trascrizione dei geni della firma associata allo stress. Inoltre, si è visto che iCAF è la principale tipologia cellulare del microambiente tumorale che esprime ligandi (ad esempio IL6, CXCL12 e LIF) che promuovono cambiamenti immunosoppressivi ad esempio nei macrofagi.

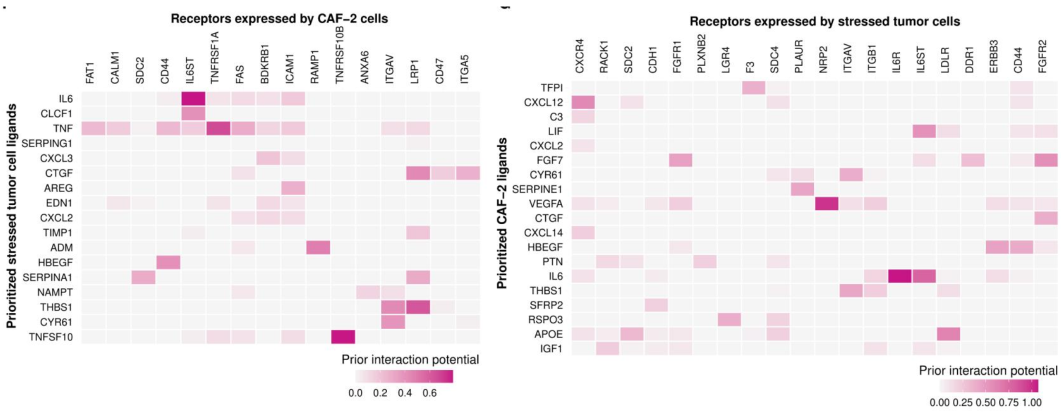

Figura 9: *Heatmap* che mostrano le interazioni recettore-ligando. In particolare, quella di sinistra considera i ligandi nelle cellule tumorali ad alto stress e i recettori espressi da iCAF, e quella di destra considera le interazioni tra i ligandi negli iCAF e i recettori espressi dalle cellule tumorali ad alto stress. La gradazione di colore è proporzionale all'effetto che ha quell'interazione sull'espressione genica delle cellule coinvolte.
Fonte: Longitudinal single-cell RNA-seq analysis reveals stress-promoted chemoresistance in metastatic ovarian cancer - Supplementary materials

Il ruolo di TNF e IL6 prodotti dalle cellule del microambiente tumorale è stato studiato anche in altri tumori, come ad esempio quello al seno, quello alla prostata e quello al colon-retto.

4. Conclusioni

Zhang *et al.* hanno definito uno stato trascrizionale associato allo stress nelle cellule tumorali di pazienti HGSOC, il quale è predittore dello sviluppo della resistenza alla chemioterapia, e hanno identificato dei possibili marcatori di stato trascrizionale. In futuro, potrebbero essere pianificati dei *clinical trial* per verificale l'effettiva applicabilità di questi marcatori nella pratica clinica.

Gli autori hanno anche dimostrato che le cellule tumorali ad alto stress sono correlate alla presenza di macrofagi e linfociti CD8+ in stati trascrizionali immunosoppressivi. Inoltre, hanno evidenziato come il TNF e l'IL-6 prodotti dalle cellule tumorali ad alto stress e dagli iCAF promuovano un ciclo paracrino di tipo *feed-forward* che induce tali stati trascrizionali in entrambi i tipi cellulari. Quest'ultima osservazione apre la strada per lo sviluppo di immunoterapie che vadano a bersagliare questa via di segnalazione paracrina, permettendo così di superare la resistenza alla chemioterapia. Ulteriori studi potrebbero verificare se alcuni fattori di stress ambientale possono alterare il microambiente tumorale, e quindi promuovere la chemioresistenza.

Zhang *et al.* hanno descritto in modo chiaro ed accurato le metodiche da loro utilizzate, tuttavia, esaminando il lavoro, sono emerse delle criticità riguardanti la riproducibilità delle analisi. La prima è dovuta alla presenza di restrizioni di accesso ai dati grezzi del scRNA-seq (https://ega-archive.org/datasets/EGAD00001006922) e ai dati grezzi del *bulk* RNA-seq (https://ega-archive.org/datasets/EGAD00001006456), depositati nell'*European Genome-phenome Archive* (EGA). La seconda è dovuta al fatto che non è stato pubblicato il codice R utilizzato per analizzare i dati.

Bibliografia

1. Oronsky, B., Ray, C.M., Spira, A.I. et al. A brief review of the management of platinum-resistant–platinum-refractory ovarian cancer. *Med Oncol* **6**, 103 (2017). https://doi.org/10.1007/s12032-017-0960-z

2. See, P., Lum, J., Chen, J., Ginhoux, F. A Single-Cell Sequencing Guide for Immunologists. *Front. Immunol.* **9**, 2425 (2018). https://doi.org/10.3389/fimmu.2018.02425

3. Illumina. An introduction to Next-Generation Sequencing Technology. 2017. (https://www.illumina.com/content/dam/illumina-marketing/documents/products/illumina_sequencing_introduction.pdf).

4. You, Y., Tian, L., Su, S. et al. Benchmarking UMI-based single-cell RNA-seq preprocessing workflows. *Genome Biol* **22**, 339 (2021). https://doi.org/10.1186/s13059-021-02552-3

5. 10X Genomics. Chromium Single Cell 3’ Reagent Kits v2 User Guide. 2019. (https://assets.ctfassets.net/an68im79xiti/RT8DYoZzhDJRBMrJCmVxl/6a0ed8015d89bf9602128a4c9f8962c8/CG00052_SingleCell3_ReagentKitv2UserGuide_RevF.pdf)

6. Yang, L., Xie, H., Li, Y. et al. Molecular mechanisms of platinum-based chemotherapy resistance in ovarian cancer. *Oncol Rep* **47**, 4 (2022). https://doi.org/10.3892/or.2022.8293

7. Luyckx, M., Luyckx, J., Bruger, A. et al. Ovarian Cancer. *Exon Publications*. ISBN: 978-0-645-33208-7 (2022). http://www.ncbi.nlm.nih.gov/books/NBK585985/

8. Illumina. Single-Cell Sequencing Workflow: Critical Steps and Considerations. 2019. (https://www.illumina.com/content/dam/illumina-marketing/documents/products/other/single-cell-sequencing-ebook-770-2019-007.pdf).

9. https://gco.iarc.fr/today/data/factsheets/cancers/39-All-cancers-fact-sheet.pdf

10. https://gco.iarc.fr/today/data/factsheets/cancers/25-Ovary-fact-sheet.pdf

Appendice

Articolo presentato e discusso in questo elaborato:

Kaiyang Zhang, Erdogan Pekcan Erkan, Sanaz Jamalzadeh, Jun Dai, Noora Andersson, Katja Kaipio, Tarja Lamminen, Naziha Mansuri, Kaisa Huhtinen, Olli Carpén, Sakari Hietanen, Jaana Oikkonen, Johanna Hynninen, Anni Virtanen, Antti Häkkinen, Sampsa Hautaniemi, Anna Vähärautio. Longitudinal single-cell RNA-seq analysis reveals stress-promoted chemoresistance in metastatic ovarian cancer. *Sci Adv* **8**, 8 (2022). https://doi.org/10.1126/sciadv.abm1831

CANCER

Longitudinal single-cell RNA-seq analysis reveals stress-promoted chemoresistance in metastatic ovarian cancer

Kaiyang Zhang[1], Erdogan Pekcan Erkan[1], Sanaz Jamalzadeh[1], Jun Dai[1], Noora Andersson[1], Katja Kaipio[2], Tarja Lamminen[2], Naziha Mansuri[2], Kaisa Huhtinen[2], Olli Carpén[1,2,3], Sakari Hietanen[4], Jaana Oikkonen[1], Johanna Hynninen[4], Anni Virtanen[5,6], Antti Häkkinen[1], Sampsa Hautaniemi[1]*, Anna Vähärautio[1]*

Chemotherapy resistance is a critical contributor to cancer mortality and thus an urgent unmet challenge in oncology. To characterize chemotherapy resistance processes in high-grade serous ovarian cancer, we prospectively collected tissue samples before and after chemotherapy and analyzed their transcriptomic profiles at a single-cell resolution. After removing patient-specific signals by a novel analysis approach, PRIMUS, we found a consistent increase in stress-associated cell state during chemotherapy, which was validated by RNA in situ hybridization and bulk RNA sequencing. The stress-associated state exists before chemotherapy, is subclonally enriched during the treatment, and associates with poor progression-free survival. Co-occurrence with an inflammatory cancer–associated fibroblast subtype in tumors implies that chemotherapy is associated with stress response in both cancer cells and stroma, driving a paracrine feed-forward loop. In summary, we have found a resistant state that integrates stromal signaling and subclonal evolution and offers targets to overcome chemotherapy resistance.

INTRODUCTION

Platinum-based chemotherapy is the most widely prescribed drug in metastatic cancer treatment (*1*). It is curative in testicular cancers and effective in other cancers, such as in high-grade serous ovarian cancer (HGSOC) where the introduction of platinum-based combination therapy improved the 10-year survival rate by more than 10% and doubled the number of complete responses (*1*, *2*). However, most patients with HGSOC develop platinum resistance leading to almost invariably fatal refractory disease and only 43% 5-year survival (*3*). HGSOC is a copy number–driven cancer that has exceptionally high intratumor heterogeneity and almost 100% prevalence of *TP53* mutations (*4*, *5*), which impedes overcoming platinum resistance.

Patients with platinum-sensitive HGSOC with homologous recombination–deficient (HRD) tumors benefit from poly(adenosine diphosphate–ribose) polymerase (PARP) inhibitors (*6*). However, approximately half of the patients with HGSOC do not have HRD tumors and face very limited treatment options at the chemotherapy-resistant stage. On cellular level, clinically observed chemotherapy resistance is a continuum from a Darwinian selection process of intrinsically resistant cell populations to an adaptive induction of a fitness phenotype (*7*, *8*). Most studies of drug resistance in the clinical setting have so far focused on genetic changes, such as *MET* amplification with kinase inhibitors (*9*), *BRCA* reversal mutations with chemotherapy (*10*), or genomic signatures in a heterogeneously treated patient cohort (*11*). The number and complexity of resistance mechanisms to chemotherapy surpass those of targeted therapies (*12*), which warrant homogeneously treated patient cohorts that allow high-resolution analysis of cancer cells before and after chemotherapy.

Chemotherapy affects transcriptional programs of cancer cells, which provides an opportunity to comprehensively decipher the most relevant chemotherapy-induced processes using single-cell RNA sequencing (scRNA-seq) data. Data from scRNA-seq also enable addressing the interplay between cancer cells and tumor microenvironment (TME). scRNA-seq and genomic analysis performed before and after treatment in paired samples from four patients with metastatic breast cancer revealed that while chemotherapy selected preexisting genetic abnormalities, it also induced adaptive transcriptional changes related to epithelial-to-mesenchymal transition (EMT), *AKT1* signaling, and hypoxia (*13*). In paired samples from four patients with non–small cell lung cancer, the surviving cells underwent a primitive state change to alveolar cells in residual disease (*14*). While these studies demonstrate the importance of paired samples, they each had cancer cells containing pairwise specimens from only four patients and, more importantly, limited clinical data from the patients, such as the patient outcome after therapy or survival times, which hinders making clinically relevant conclusions from the data.

Here, we characterized transcriptional patterns of chemotherapy resistance in HGSOC using patient-derived prospective tissue sample pairs before and after treatment at single-cell resolution. Our cohort consists of scRNA-seq data from treatment-naïve and post–neoadjuvant chemotherapy (post-NACT) pairs from 11 homogeneously treated patients with HGSOC with full clinical information. To validate our findings, we used RNA in situ hybridization (RNA-ISH) data of 10 treatment-naïve versus post-NACT sample pairs, 49 bulk RNA-seq samples including 18 treatment-naïve versus post-NACT

[1] Research Program in Systems Oncology, Research Programs Unit, Faculty of Medicine, University of Helsinki, Helsinki, Finland. [2] Cancer Research Unit, Institute of Biomedicine and FICAN West Cancer Centre, University of Turku, Turku, Finland. [3] Department of Pathology, University of Helsinki and HUSLAB, Helsinki University Hospital, Helsinki, Finland. [4] Department of Obstetrics and Gynecology, University of Turku and Turku University Hospital, Turku, Finland. [5] Finnish Cancer Registry, Helsinki, Finland. [6] Department of Pathology, University of Helsinki and HUS Diagnostic Center, Helsinki University Hospital, Helsinki, Finland.
*Corresponding author. Email: sampsa.hautaniemi@helsinki.fi (S.H.); anna.vaharautio@helsinki.fi (A.Vä.)

pairs, and 8 treatment-naïve versus relapse pairs in the HERCULES cohort (http://project-hercules.eu/) and bulk RNA-seq data of 271 treatment-naïve samples in The Cancer Genome Atlas (TCGA) cohort (*5*). Our unbiased analysis reveals how chemotherapy modulates cancer cell states by both subclonal selection and microenvironment-boosted transcriptional induction across the homogeneously treated sample cohort. Our results define a cell state that allows biomarker-based prediction and targeting of chemoresistance.

RESULTS

Obtaining scRNA-seq data from HGSOC patient samples before and after chemotherapy

We collected prospective tissue samples from 11 patients with HGSOC before and after chemotherapy and measured transcriptomes of 93,650 cells using scRNA-seq (Fig. 1A and see Materials and Methods). All patients in the study were treated with NACT, i.e., diagnostic laparoscopy followed by three cycles of platinum-taxane, interval debulking surgery (IDS), and adjuvant chemotherapy, and four patients further received bevacizumab maintenance therapy. NACT is typically recommended for patients who are inoperable at diagnosis and often have poor prognosis. Accordingly, in our cohort, the median platinum-free interval (PFI; Fig. 1A), which measures the time from treatment end to relapse, is only 4.2 months. Our sample cohort with metastatic tumors from poorly responsive patients represents many understudied aspects of HGSOC as described in Materials and Methods. Further clinical information of the cohort is given in Table 1.

After quality control (see Materials and Methods and fig. S1, A to D), we obtained a total of 51,786 cells, including 8806 malignant epithelial (tumor), 8045 stromal, and 34,935 immune cells for the subsequent analyses. We identified epithelial, stromal, and immune

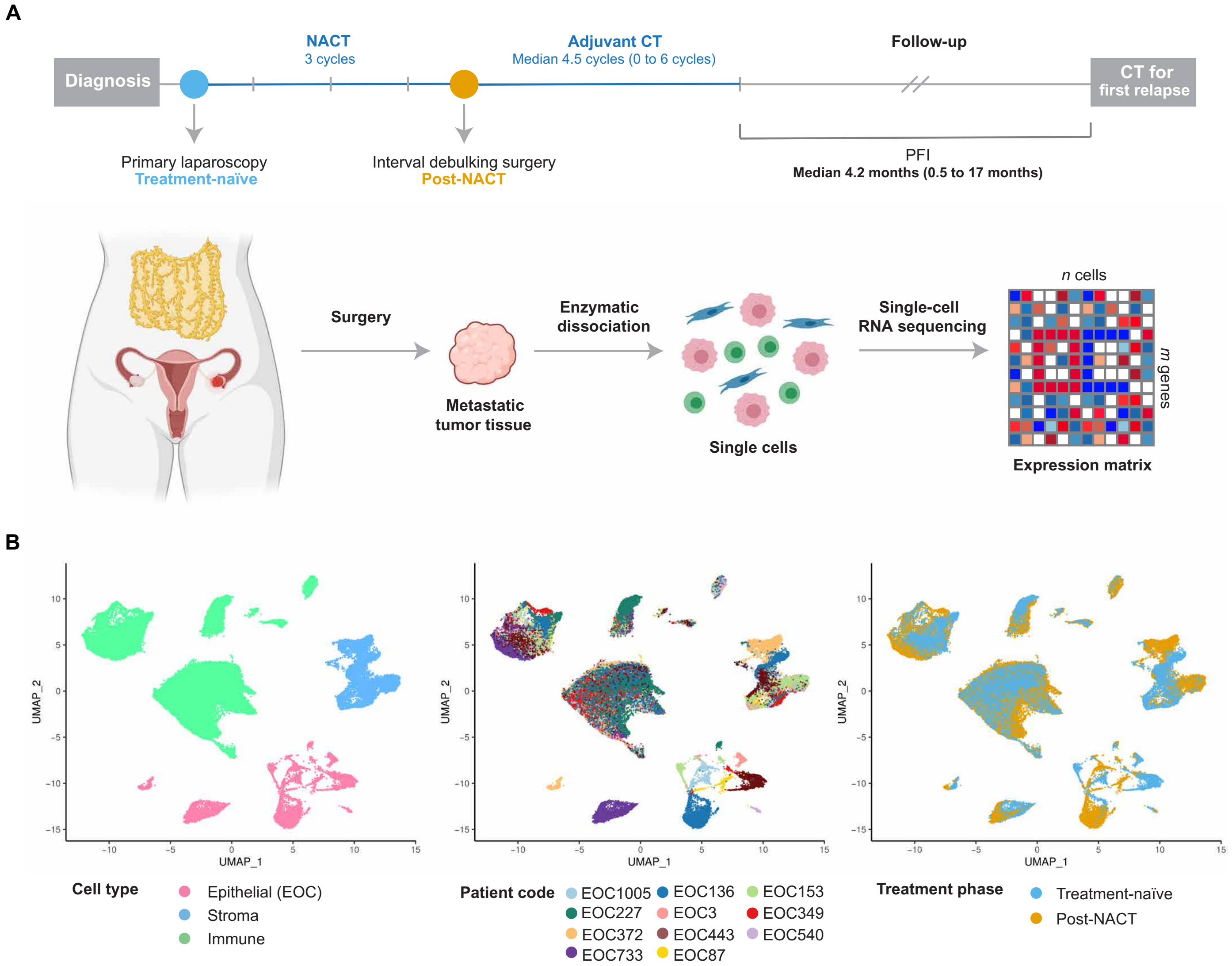

Fig. 1. Overview of experimental and sequencing workflow. (**A**) Diagram showing the sample collection and processing. We collected prospective tumor samples from 11 patients with HGSOC before and after NACT. The median PFI in the cohort was 4.2 months. scRNA-seq was performed on dissociated solid tumor specimens using the 10x Genomics Chromium platform. (**B**) Uniform manifold approximation and projection (UMAP) plot of all cells ($n = 51,786$) passing the quality control, colored by cell type, patient code, and treatment phase. EOC, epithelial ovarian carcinoma.

Table 1. Patient and sample information. PDS, primary debulking surgery; NA, not available; CRS, chemotherapy response score; TN, treatment-naïve; PN, post-NACT.

Patient ID	Age[*]	Treatment	Stage[†]	PFI (days)	CRS	CA125 (U/ml)		Anatomical locations[‡]				
						TN	PN	scRNA-seq TN	scRNA-seq PN	Bulk RNA-seq TN	Bulk RNA-seq PN	Bulk RNA-seq relapse
EOC1005	73	NACT	IVA	65	2	3776	343	Peritoneum	Tumor[§]	NA	NA	NA
EOC136	64	NACT	IVA	520	2	2647	212	Mesentery	Omentum	NA	NA	NA
EOC153	78	NACT	IVA	393	2	1063	93	Omentum	Omentum	NA	NA	NA
EOC227	74	NACT	IVA	230	2	445	33	Omentum[§]	Omentum[§]	NA	NA	NA
EOC3	67	NACT	IVA	14	2	821	221	Peritoneum[§]	Omentum	Peritoneum	Omentum	NA
EOC349	67	NACT	IVB	36	2	2155	67	Peritoneum[§]	Omentum[§]	NA	NA	NA
EOC372	68	NACT	IIIC	460	1	3180	334	Peritoneum	Peritoneum	Peritoneum	Peritoneum	NA
EOC443	54	NACT	IVA	177	3	2295	82	Omentum	Omentum	Omentum	Omentum	NA
EOC540	62	NACT	IIIC	126	2	155	7	Omentum	Omentum	NA	NA	NA
EOC733	72	NACT	IVA	83	1	22079	3579	Peritoneum	Omentum	NA	NA	NA
EOC87	62	NACT	IIIC	30	1	998	346	Peritoneum	Omentum	Omentum	Omentum	NA
EOC1129	75	NACT	IIIC	210	NA	3493	212	NA	NA	Omentum	Mesentery	NA
EOC160	68	PDS	IVB	648	NA	145	NA	NA	NA	Omentum	NA	Mesentery
EOC183	68	NACT	IIIC	203	2	411	15	NA	NA	Omentum	Omentum	NA
EOC218	71	NACT	IIIC	974	2	2633	38	NA	NA	Omentum	Omentum	NA
EOC26	72	NACT	IIIC	0	2	553	55	NA	NA	Omentum	Omentum	Ascites
EOC376	67	NACT	IIIC	280	1	615	20	NA	NA	Omentum	Omentum	NA
EOC423	81	NACT	IIIC	721[‖]	2	854	20	NA	NA	Omentum	Ovary	NA
EOC568	57	NACT	IVA	210	3	192	70	NA	NA	Mesentery	Omentum	NA
EOC587	71	NACT	IVB	27	3	149	22	NA	NA	Peritoneum	Tumor	NA
EOC649	77	NACT	IVB	511	2	588	22	NA	NA	Peritoneum	Omentum	NA
EOC677	68	NACT	IIIC	81	2	1593	11	NA	NA	Peritoneum	Peritoneum	Ascites
EOC883	74	NACT	IIIC	91	NA	1515	NA	NA	NA	Adnexa	Ascites	NA
EOC891	71	NACT	IIIC	183	NA	687	NA	NA	NA	Omentum	NA	Ascites
EOC933	74	NACT	IIIC	632	3	296	13	NA	NA	Peritoneum	Mesentery	NA
EOC868	62	NACT	IIIC	285	2	1565	36	NA	NA	Peritoneum	Omentum	Peritoneum
EOC1133	66	NACT	IVB	661	2	1156	22	NA	NA	Peritoneum	Omentum	NA
EOC167	75	NACT	IIIC	19	NA	5614	NA	NA	NA	Omentum	NA	Ascites
EOC295	66	NACT	IIIC	221	2	320	74	NA	NA	Peritoneum	NA	Ascites
EOC752	64	NACT	IIIC	174	2	2341	58	NA	NA	Peritoneum	NA	Ascites

*Age at diagnosis, years. †Tumor staging was performed according to the International Federation of Gynecology and Obstetrics 2014 guidelines. ‡Anatomical locations from which the samples were collected for analyses. §Cell suspension was stored as frozen before scRNA-seq processing. ||No progression, PFI at outcome update.

cells based on graph-based clustering (*15*) and acknowledged markers (fig. S1B). In contrast to stromal and immune cells, where cells from different patients grouped together, cancer cells exhibited a patient-specific expression pattern (Fig. 1B), similar to previous studies (*14*, *16*, *17*).

PRIMUS identifies phenotypic groups from heterogenous scRNA-seq datasets

The observed strong interpatient heterogeneity in cancer cells from genetically divergent cancer samples impedes the direct comparison of transcriptomes across patients. To address this challenge, we developed PRIMUS (Poisson scRNA integration of mixed unknown signals), a holistic clustering approach that identifies phenotypic cell groups from the scRNA-seq data while accounting for patient-specific components and technical noise (Fig. 2A). Specifically, as input, PRIMUS takes scRNA-seq datasets from multiple patients, a design matrix encoding the different nuisance factors, such as patient labels, technical factors (e.g., scRNA-seq quality control metrics), and a vector of size factors. PRIMUS then uses a bilinear Poisson regression model to simultaneously factorize the expression data into the defined nuisance factors, undefined cellular phenotypes, and their corresponding transcriptomic profiles (see Materials and Methods and the Supplementary Materials). As a statistical model, PRIMUS also allows the selection of an optimal number of clusters based on Bayesian information criterion (BIC).

We compared the performance of PRIMUS with existing integration methods (*15*, *18*–*23*) on simulated data and multistudy pancreatic datasets (fig. S2). We simulated datasets containing five cell groups from six samples with different genetic backgrounds and sample-specific effects using splatPop (*24*, *25*) under three scenarios (table S1): (i) All six samples contain the five cell groups; (ii) each sample only contains a subset of cell groups, three pairs of samples had no cell groups in common, and there was one sample-specific cell group; and (iii) the same setting with scenario ii but with unbalanced cell numbers in each sample (from 20 to 2000). For all simulated scenarios and for the pancreatic datasets, PRIMUS was able to accurately cluster cells based on latent cell groups across different samples (fig. S2, A to H). It showed similarly good performance as other existing methods in scenario i, where all samples have the same cell group composition, and performed better than other methods in scenarios ii and iii as well as the real pancreatic datasets, which present sample-specific cell groups/types, and some samples do not have any cell groups/types in common (fig. S2I).

Our results from simulated and pancreatic datasets show that PRIMUS can accurately cluster cells by phenotypic groups, accounting for data source–specific effects from distinct samples. Unlike existing methods, PRIMUS is robust to heterogeneous cell compositions and unbalanced number of cells in different sources, and it also preserves data source–specific cell groups if such are present. Therefore, PRIMUS is a well-justified choice for clustering datasets with potentially unbalanced presentation of phenotypic groups, such as cancer cell states within heterogeneous tumor specimens.

Identification and characterization of cancer cell states in HGSOC

By using PRIMUS to control the effect of patient-specific variability and technical confounders, such as the percentage of unique molecular identifier (UMI) counts originating from mitochondrial genes, we identified 12 cancer cell clusters (fig. S3A), including three patient-specific clusters (C3, C9, and C10) and nine shared clusters across multiple patients (Fig. 2, B and C). The proportion and number of cells in each cluster from each patient are presented in fig. S3 (B and C, respectively).

To characterize the identified cancer cell clusters, we first identified 4742 significantly differentially expressed genes (DEGs) between at least one pair of the 12 clusters using a likelihood-ratio test (LRT) [false discovery rate (FDR) < 0.01; see Materials and Methods]. To construct well-annotated gene coexpression signatures, we built a gene network using the DEGs integrated to a gene annotation database (*26*) and identified 10 distinct gene signatures after filtering (see Materials and Methods, Fig. 2C, and fig. S3D). Four of 12 clusters (C1, C2, C6, and C12) had no overrepresented gene signatures, suggesting that their DEGs were incoherent, with only limited coexpression and/or poorly annotated, and were thus excluded from further analysis. The remaining eight clusters were characterized by the 10 distinct gene signatures (Fig. 2C and fig. S3E).

Pathway analysis showed that the 10 signatures were associated with diverse biological processes (Fig. 2D). These include key processes previously identified in HGSOC tumors, such as differentiation in cluster C4, proliferation and DNA repair in cluster C5, and EMT identified in the patient-specific cluster C3 (*5*, *27*). We also identified a major histocompatibility complex (MHC) class II antigen presentation signature with high *HLA-DPA1*, *HLA-DQA1*, and *HLA-DRA* expression in the patient-specific cluster C10. Although MHC class II expression is classically considered a feature of professional antigen presenting immune cells, it was recently identified in single HGSOC and normal fallopian tube epithelial cells by Izar *et al.* (*28*) and Hu *et al.* (*27*). Aforementioned studies also identified signatures associated with stress response but excluded them from further analysis as likely artefactual. In our dataset, stress-associated signature, overexpressed by cluster C7, not only consisted of stress-responsive immediate early genes (IEGs) (e.g., *CEBPB*, *FOS*, and *JUN*) but also contained proinflammatory cytokines and receptors [e.g., *IL6*, *TNF*, and *CXCR4*], core transcriptomic regulators of EMT (e.g., *SNAI1* and *SNAI2*), and stemness (*HES1* and *ID2*), as well as prosurvival (e.g., *GADD45B*, *GADD45G*, and *MCL1*) and antiproliferative (*CDKN1A*) genes. Notably, many genes in this signature, such as *IL6*, *TNF*, *CEBPD*, *ATF3*, *NFKBIA*, *BCL6*, *GADD45B*, *GADD45G*, *MCL1*, and *CDKN1A*, are targets of the transcription factor nuclear factor κB (NF-κB). In addition to the cluster-specific signatures described above, we identified three metabolism-associated signatures that were shared by several clusters, representing tricarboxylic acid cycle (TCA), proteasomal degradation, and RNA processing (Table 2).

Chemotherapy affects the prevalence of proliferative and stress-associated cancer cell populations

To test the effect of chemotherapy on the identified 12 cancer cell clusters, we examined the fractional changes of the five clusters that contained cells from multiple patients during chemotherapy. Here, we observed significant differences only in the fractions of the populations expressing proliferative DNA repair signature (C5, $P = 0.014$) and the stress-associated signature (C7, $P = 0.002$) between treatment-naïve and post-NACT samples (Fig. 3A).

The significant decline of C5 cells, from an average of 14% in treatment-naïve samples to an average of 3% in post-NACT samples, implies that chemotherapy either kills most of the proliferative cells

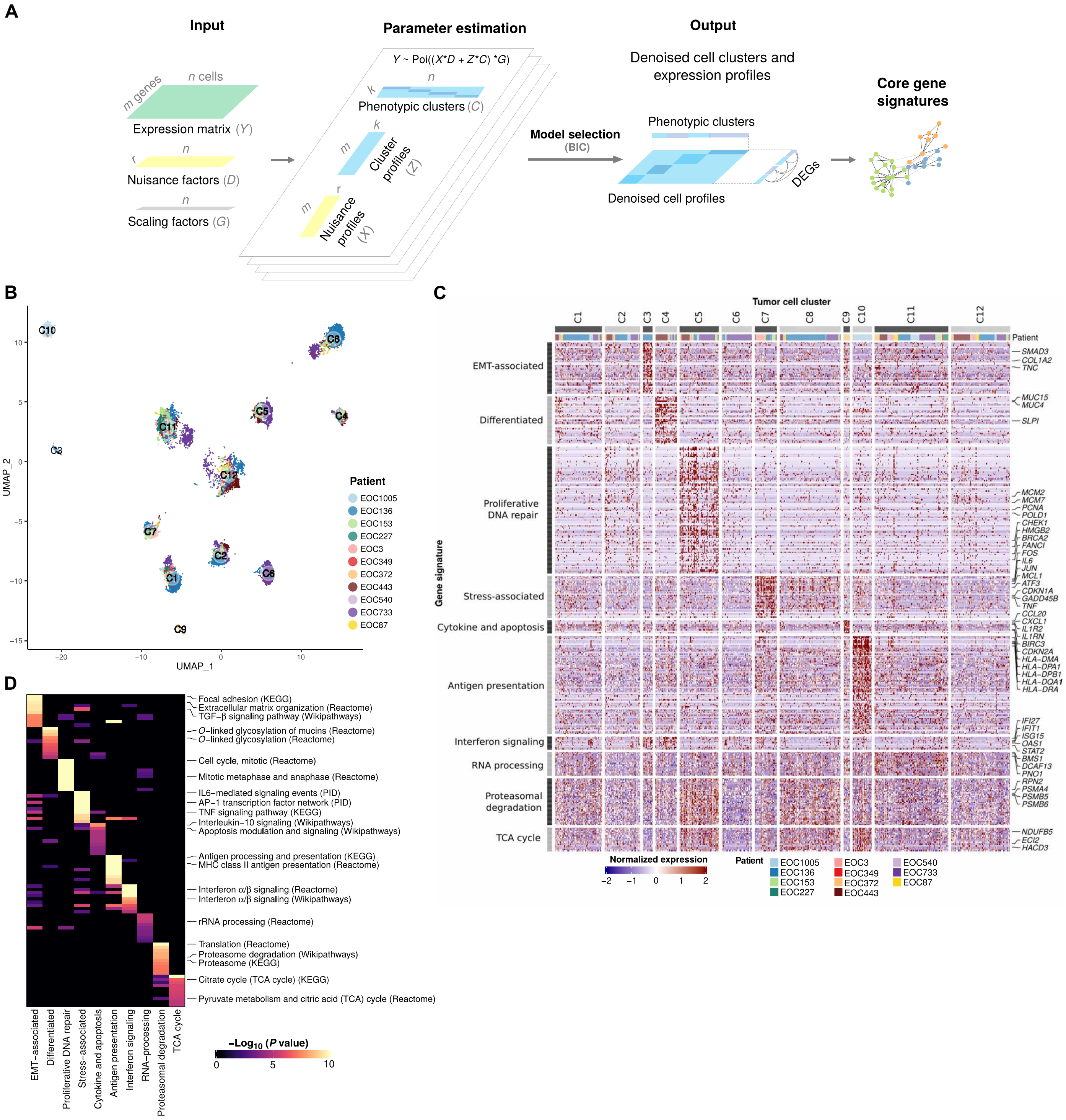

Fig. 2. Identification of 12 subpopulations of HGSOC cancer cells characterized by 10 gene signatures. (**A**) Schematic of the PRIMUS model. PRIMUS models the observed single-cell expression profiles (Y) as a mixture of latent phenotypic cluster profiles and nuisance profiles. Given Y, the known nuisance factors D, known size factors G, and the number of latent phenotypic clusters k, PRIMUS estimates the latent nuisance profiles X, latent phenotypic cluster profiles Z, and the latent cluster memberships C using an expectation-maximization (EM) algorithm. (**B**) UMAP plot of cancer cells after removing the nuisance signals, colored by patient and labeled by the identified clusters. (**C**) Heatmap of the expression of the 10 distinct gene signatures in the 12 identified cell clusters. Rows correspond to genes and columns to cells. (**D**) Heatmap shows the top 10 pathways enriched in each gene signature. TGF-β, transforming growth factor–β; AP1, activating protein 1; TNF, tumor necrosis factor; rRNA, ribosomal RNA; KEGG, Kyoto Encyclopedia of Genes and Genomes; PID, the Pathway Interaction Database.

Table 2. Annotation of tumor cell clusters.

Cell cluster	Characteristic gene signature	Representative pathways	Marker genes
C3	EMT-associated (43 genes)	TGF-β signaling pathway, focal adhesion	*SMAD3, COL1A2, TNC*
C4	Differentiated (40 genes)	*O*-linked glycosylation of mucins	*MUC4, MUC16, SLPI*
C5	Proliferative DNA repair (106 genes)	Cell cycle, DNA repair, Homology directed repair (HDR) through homologous recombination, Fanconi anemia pathway	*PCNA, CHEK1, HMGB2, BRCA2, FANCI, POLD1*
C7	Stress-associated (35 genes)	IL6-mediated signaling events, TNF signaling pathway, cellular responses to stress	*JUN, FOS, IL6, TNF, CXCR4, SNAI1, VIM, GADD45B, MCL1*
C9	Cytokine and apoptosis (11 genes)	IL10 signaling, apoptosis modulation and signaling	*CXCL1, CCL20, IL1R2, BIRC3, CDKN2A, BIK*
C10	Antigen presentation (82 genes)	Antigen processing and presentation, MHC class II antigen presentation	*HLA-DPA1, HLA-DQA1, HLA-DRA*
C3, C4	Interferon signaling (11 genes)	Interferon signaling	*STAT2, IFI27, IFIT1, OAS1, ISG15*
C3, C11	RNA processing (20 genes)	rRNA processing, apoptotic cleavage of cellular proteins	*DCAF13, PNO1, BMS1, ACIN1, TJP1, ROCK1*
C5, C8	Proteasomal degradation (39 genes)	Proteasome degradation, proteasome complex	*PSMA4, PSMB5, PSMB6, RPN2*
C5, C8, C10	TCA cycle (20 genes)	Citrate cycle (TCA cycle), pyruvate metabolism	*HACD3, NDUFB5, ECI2*

or induces cell cycle arrest. An interesting exception to this was patient EOC87 whose fraction of proliferative cells increased from 7 to 11% during chemotherapy. The patient showed no histopathologic response to chemotherapy in omentum and poor prognosis with an overall survival (OS) of only 9 months. This poor prognosis was unexpected since she had a somatic, heterogeneous *BRCA2* frameshift deletion (c.1338delG), which is classified in ClinVar (*29*) as likely pathogenic and thus should be indicative of good response to platinum and PARP inhibitors.

The cluster (C7) represented by stress-associated signature was enriched from an average of 3% in treatment-naïve samples to an average of 17% in post-NACT samples, indicating that this cell state was induced and/or more likely to survive through chemotherapy. We further computed a stress score using stress-associated signature (35 genes) for cancer cell–specific expression deconvoluted from bulk RNA-seq data of 18 treatment-naïve versus post-NACT pairs and 8 treatment-naïve versus relapse pairs. Consistently, post-NACT ($P = 0.0034$) and relapse ($P = 0.0078$) samples showed significantly higher stress scores in comparison to treatment-naïve samples (Fig. 3B). Patient EOC87 with a *BRCA2* frameshift deletion and progressive disease after NACT had the highest stress-associated cluster fraction in the treatment-naïve samples (7%), which may partly explain her poor response to chemotherapy.

Validation of the stress signature with RNA-ISH

To validate the stress-associated signature with an independent measurement technology, we quantified the expression of 10 stress signature genes in 10 treatment-naïve and post-NACT HGSOC sample pairs with RNA-ISH experiments (see Fig. 3C for representative images). We used canonical correlation analysis (CCA) (see Materials and Methods) to define a stress score that is an aggregate of the RNA-ISH expression levels of the 10 genes to quantify the stress status of each sample.

The RNA-ISH stress score was significantly correlated ($R = 0.81$, permutation test, $P < 10^{-5}$) with the scRNA-seq stress score in the matched samples (Fig. 3D). Moreover, the post-NACT samples had significantly higher RNA-ISH stress scores in comparison with the treatment-naïve samples (Fig. 3E; permutation test, $P = 0.00124$), confirming the increase in the stress-associated signature after chemotherapy.

Stress-associated state is subclonally enriched during chemotherapy

To assess the effect of subclonal variation on the level of the stress-associated state, we used scRNA-seq data estimated copy number alteration (CNA) profiles to infer the subclonal structure of each patient (*30*). The subclonal CNA profiles inferred from scRNA-seq data had good concordance with subclonal CNA profiles obtained from the bulk whole-genome sequencing data from the same patients (Spearman's correlation coefficient of 0.44 to 0.81; fig. S4A). Figure 4 (A and B) shows the inferred CNA subclonal structure of two representative patients: patient EOC3 with progressive disease and a PFI of only 14 days and patient EOC136 with complete response and a long PFI of 520 days. Both received standard NACT, had carcinosis after IDS, and neither participated in clinical trials nor received bevacizumab maintenance treatment. The subclones in EOC3 had generally higher stress scores than EOC136 in treatment-naïve samples, whereas the subclonal distances were longer for EOC3, indicating that, unexpectedly, the poor-response patient had lower level of genetic heterogeneity. In both patients, the subclones with higher stress scores in treatment-naïve samples were expanded more than low-stress subclones after

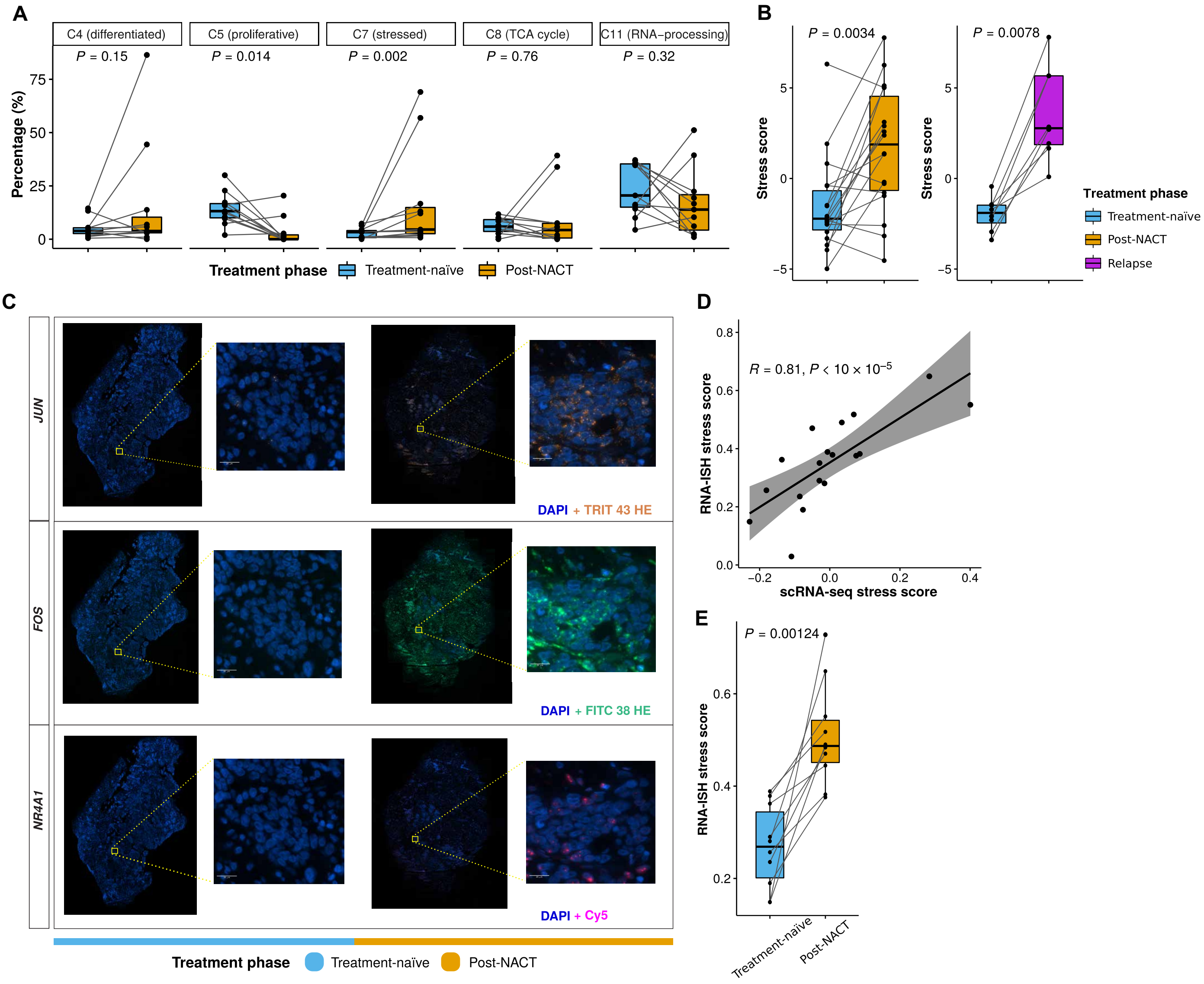

Fig. 3. Stress-associated transcriptional profile is enriched after chemotherapy. (**A**) Boxplots showing the fractional changes of the five tumor clusters containing cells from multiple patients, between the treatment-naïve (blue) and post-NACT (yellow) samples of each patient (paired Wilcoxon rank-sum test). Horizontal bars show median values, box edges represent the interquartile range, and each dot represents a sample. (**B**) Boxplots comparing the stress scores in treatment-naïve (blue) versus post-NACT (yellow) samples (left; paired Wilcoxon rank-sum test, $P = 0.0034$), and treatment-naïve (blue) versus relapse (purple) samples (right; paired Wilcoxon rank-sum test, $P = 0.0078$) using bulk RNA-seq data from the HERCULES cohort. Horizontal bars show median values, box edges represent the interquartile range, and each dot represents a sample. (**C**) Representative RNA-ISH images showing the changes of *NR4A1*, *FOS*, and *JUN* from the treatment-naïve to post-NACT sample of patient EOC87. Scale bars, 20 μm. (**D**) Scatter plot showing the correlation ($R = 0.81$, permutation test, $P < 10 \times 10^{-5}$) between stress scores quantified using RNA-ISH and scRNA-seq experiments. Each dot represents a sample. (**E**) Boxplots comparing the RNA-ISH stress scores in treatment-naïve (blue) versus post-NACT (yellow) samples (permutation test, $P = 0.00124$). Each dot represents a sample.

chemotherapy (Fig. 4, A and B). The inferred CNA subclonality trees for all the 11 patients are shown in fig. S4B. Each patient had four to eight subclones, of which 12.5 to 100% were shared between each treatment-naïve and post-NACT sample pair. The four patients (EOC349, EOC540, EOC733, and EOC87) with all subclones shared between treatment-naïve and post-NACT samples had a median PFI of 1.99 months, indicating the limited efficacy of chemotherapy on these patients.

The inferred subclones showed significant differences in their stress scores in most patients (fig. S4B), which implies that the stress-associated state is at least partially driven by heritable differences across the subclones. Across the 11 patients studied, the subclones with the highest stress scores in treatment-naïve samples were significantly more expanded during chemotherapy when compared with the lowest-stress subclones (Fig. 4C). While the proliferation scores of the highest stress subclones remained similar, the proliferation scores of the lowest stress subclones dropped significantly after chemotherapy (Fig. 4D). This suggests that the lower ability to maintain or recover proliferation following chemotherapy contributes to the loss of stress-lowest subclones during

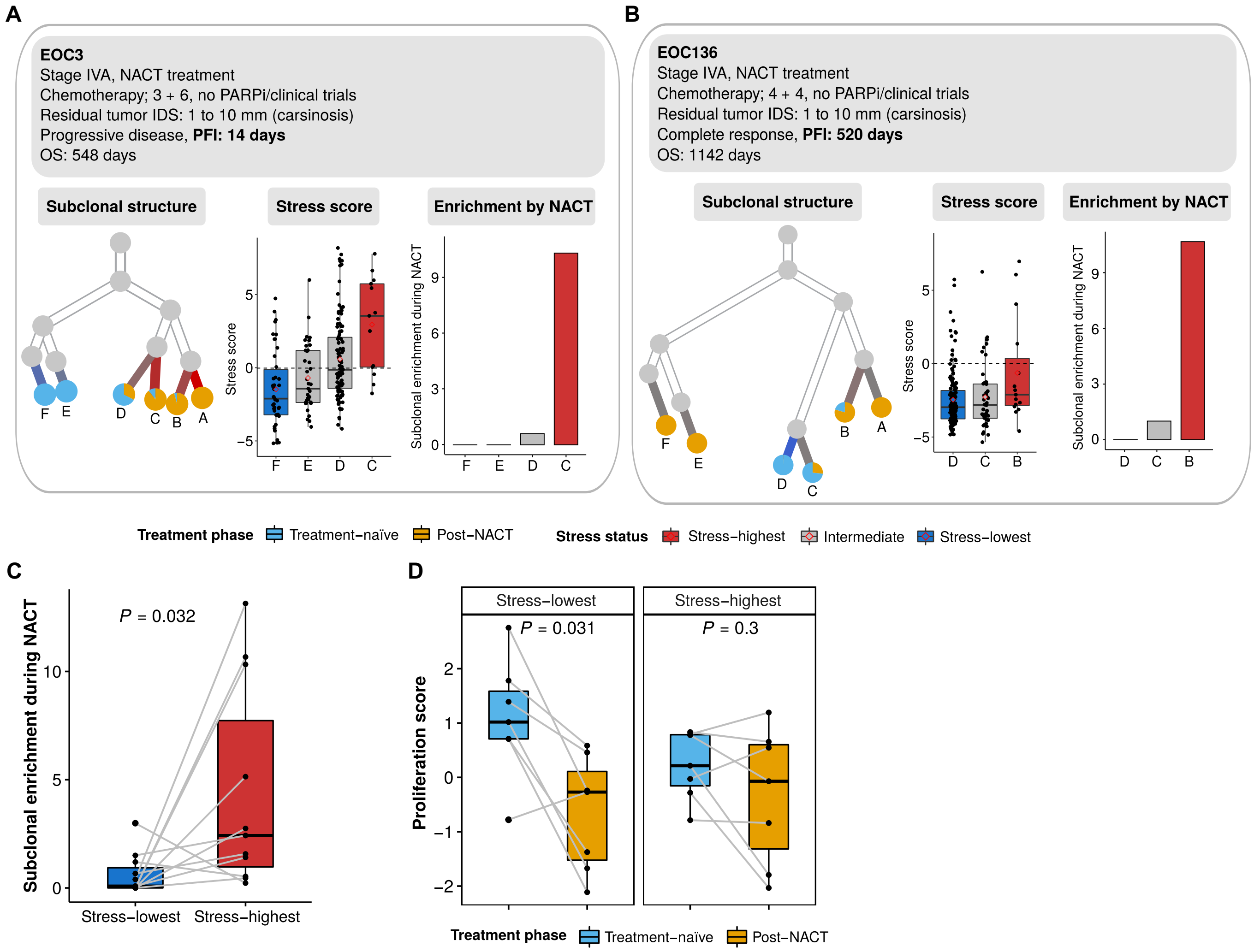

Fig. 4. Inferred CNA and subclonal analysis reveals enrichment of the stress state during chemotherapy. (**A**) Inferred clonality tree (left), subclonal stress score (middle), and subclonal enrichment during NACT (right) of a representative patient (EOC3) with progressive disease and short PFI (PFI = 14 days). Only subclones that existed in the treatment-naïve samples are included in the subclonal stress score and subclonal enrichment analysis. The subclonal enrichment is measured by the ratio of the relative abundance of post-NACT cells against the relative abundance of treatment-naïve cells. PARPi, PARP inhibitor. (**B**) Inferred clonality tree (left), subclonal stress score (middle), and subclonal enrichment during NACT (right) of a representative patient (EOC136) with progressive disease and long PFI (PFI = 520 days). (**C**) Boxplot showing the enrichment of the stress-highest (red) and stress-lowest (blue) CNA subclones during NACT. Only subclones existing in treatment naïve samples (paired Wilcoxon rank-sum test, $P = 0.032$) were included. Each dot represents a CNA subclone. (**D**) Boxplots showing the proliferation score of the stress-highest (left; paired Wilcoxon rank-sum test, $P = 0.031$) and stress-lowest (right; paired Wilcoxon rank-sum test, $P = 0.3$) CNA subclones before and after chemotherapy. Each dot represents a CNA subclone.

chemotherapy. In summary, the preexisting stress-associated state offers a selective advantage to cancer cells during chemotherapy, explained by more inert proliferation when compared to stress-low subclones.

Stress-associated transcriptional profile predicts poor prognosis in HGSOC

To investigate whether the stress-related transcriptional profile also promotes chemoresistance in treatment-naïve tumors on the patient level, we used TCGA deconvoluted bulk RNA-seq and clinical data from 271 patients (*5*, *31*). Of these, 86 patients were identified as stress-high and 144 as stress-low based on their stress scores (fig. S5A). We confirmed the high/low stress state using reverse-phase protein array data, which showed that the levels of phosphorylated c-Jun (CJUN_pS73, $P = 0.0035$) and its upstream kinase, phospho–c-Jun N-terminal kinase (JNK) (JNK_pT183Y185, $P = 0.00077$) and phosphorylated p38-α (P38_pT180Y182, $P = 0.017$), were significantly higher in the stress-high tumors compared to stress-low tumors (fig. S5B).

Kaplan-Meier survival analysis indicated that patients with stress-high tumors at diagnosis have significantly shorter progression-free survival (PFS) time (log-rank test, $P = 0.0037$; Fig. 5A). The median PFSs in stress-high and stress-low groups were 14.9 and 21.2 months, respectively. HRD is a known prognostic factor for HGSOC (*32*). Thus, we tested whether the stress-associated state can be explained by COSMIC Signature 3 (COSMIC_Sig3), which is associated with

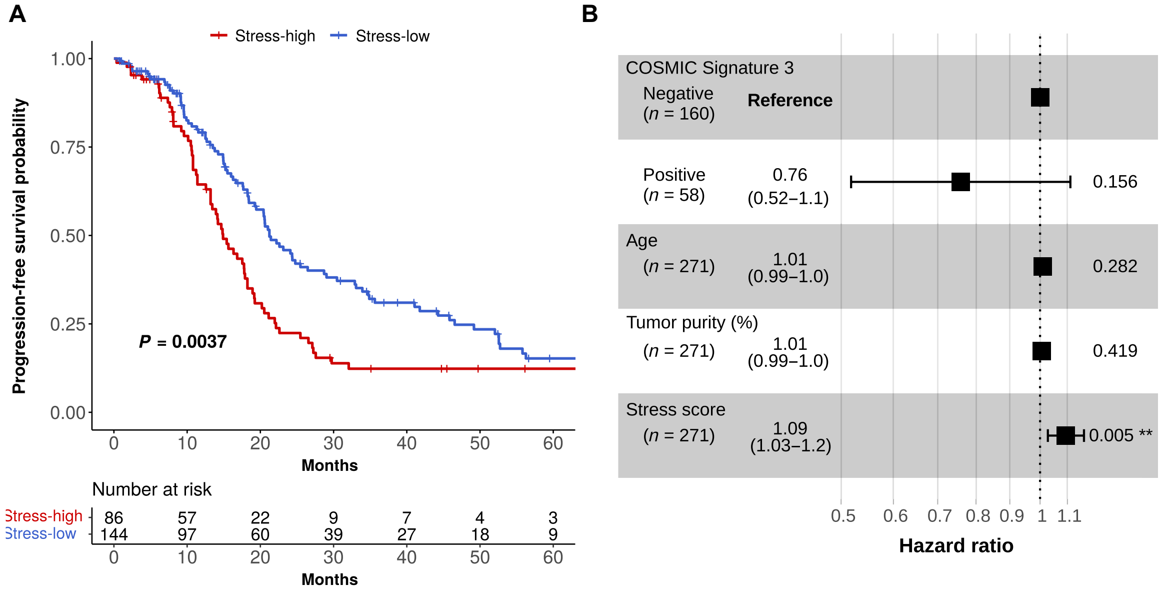

Fig. 5. Stress-associated transcriptional profile predicts poor survival in HGSOC. (**A**) Stress-high and stress-low Kaplan-Meier curves on PFS for stress-high and stress-low patients (log-rank test, $P = 0.0037$) from the TCGA cohort. The number of patients at risk is listed below the survival curves for each time point. (**B**) Forest plot showing hazard ratios, their confidence intervals, and *P* values based on a multivariate Cox proportional hazards regression model testing whether PFS relates to COSMIC Signature 3 status, age at diagnosis, tumor purity, and stress score. **: 0.001-0.01.

HRD (*33*). As shown in fig. S5C, COSMIC_Sig3 was not found enriched in stress-high or stress-low patients (Fisher's exact test, $P = 0.31$). Furthermore, multivariate Cox regression analysis showed that the stress score was significantly associated with short PFS ($P = 0.005$; Fig. 5B) independently of the effect of COSMIC_Sig3 status, age, or tumor purity. Thus, these results demonstrate that the stress-related transcriptional profile preexists in the treatment-naive tumors, and it is an independent predictor for poorly responding patients with HGSOC.

Inflammatory stroma correlates with stress-associated cancer cells

Increased expression of proinflammatory cytokines, such as *IL6* and *TNF*, in the stress-associated cancer cell population suggests that these cells could have a substantial contribution to paracrine signaling. Therefore, we set out to analyze whether stress-associated state in cancer cells was reflected in differences of TME composition and potential interactions therein.

We identified 10 immune and 5 stromal cell types based on the expression of canonical markers (Fig. 6, A and B): B cells, two types of dendritic cells (DCs), innate lymphoid cells (ILCs), macrophages, mast cells, natural killer (NK) cells, plasmacytoid DCs, plasma cells, T cells, endothelial cells, mesothelial cells, and three types of cancer-associated fibroblasts (CAFs; Fig. 6C). While none of the major immune cell types showed substantial proportional differences between stress-high and stress-low samples (fig. S6A), we set out to analyze cell state differences of the most prevalent immune cell types. Projection of T cells into a reference atlas (fig. S6, B and C) (*34*) suggested a decrease in $CD8^+$ effector memory T cells and an increase of "precursor exhausted" T cells in stress-high samples (fig. S6D). In addition, macrophages in stress-high samples exhibited significantly higher expression of immunosuppressive features (*C1QA*, *C1QB*, *C1QC*, *APOE*, and *TREM2*) (fig. S6E) ((*14*, *35*), wherein *TREM2* is functionally associated with T cell exhaustion (*36*). Together, the analyses suggest that although the cell type prevalence in immune TME is not connected with stress-associated cancer cell state per se, the stress-high samples show a shift toward compromised tumor immunity.

In line with studies from other solid cancers, HGSOC tumors contain specialized CAF subpopulations with distinct functional markers: CAF-1–expressing matrix metalloproteinases (MMPs), CAF-2–expressing inflammatory CAF (iCAF) markers *IL6*, *CXCL12*, and *LIF* (*37*), and CAF-3–expressing markers of myofibroblast identity (Fig. 6C). Trajectory analysis to explore the relations between stromal cell types shows that iCAF and CAF-1 populations form separate branches that are joined via CAF-3 and mesothelial cells (Fig. 6D). Among the stromal cell populations, only iCAFs were significantly enriched in stress-high tumors (Fig. 6E), and their markers were also strongly associated with cancer stress scores in bulk RNA-seq data (Fig. 6F). Ligand-receptor analysis to probe for potential interactions revealed that, in particular, *TNF* and its downstream effector *IL6* from stress-high cancer cells have a strong regulatory potential to induce the inflammatory phenotype of CAFs (Fig. 6G and fig. S6F). This indicates that in NACT-treated ovarian cancer, *TNF/IL6* drives the iCAF phenotype rather than *IL1B*, which has a leading role in promoting the iCAF phenotype in pancreatic cancer (*38*). In response, iCAFs produce a wide array of ligands with rich regulatory potential to activate stress-associated signature within cancer cells, including both *IL6* and *TNF* to promote a paracrine feed-forward loop (Fig. 6H and fig. S6G). Our results suggest iCAFs as the main cell type expressing *IL6*, *CXCL12*, and *LIF* in the tumor milieu, wherein these ligands promote immunosuppressive changes, such as macrophage polarization, toward the M2 phenotype (*39*).

In summary, we found that stress-associated cancer cells strongly associate with presence of iCAFs within the TME and a shift toward

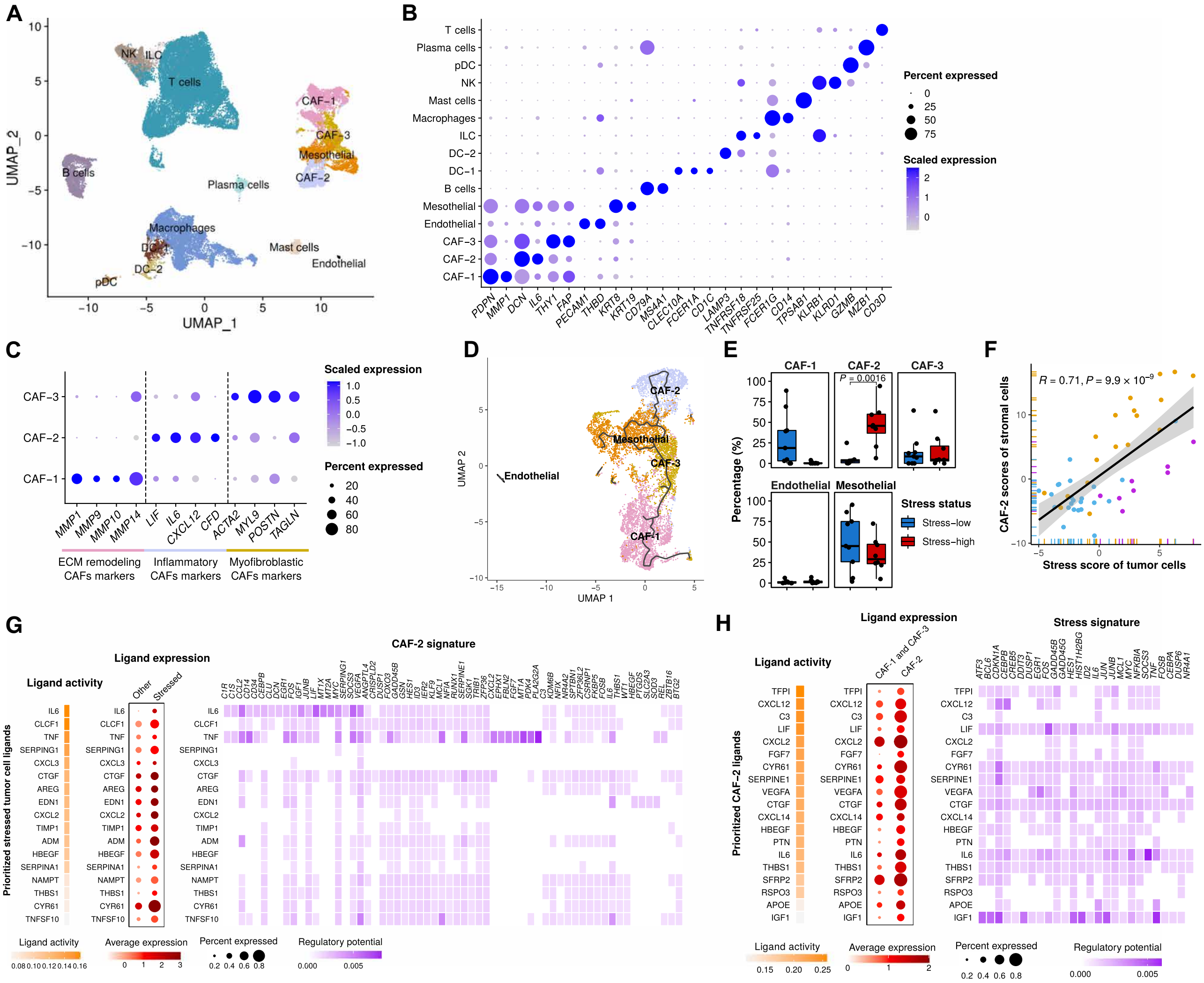

Fig. 6. Interactions between inflammatory stroma and stress-associated cancer cells. (**A**) UMAP plot of stromal and immune cells, colored by cell type. (**B**) Dot plot showing the relative expression of acknowledged stromal and immune cell subtype markers. The color intensity scale reflects the average gene expression, and the size scale indicates the percentage of cells expressing the gene within that cell type. (**C**) Dot plot showing the expression of selected marker genes of CAF subtypes. ECM, extracellular matrix. (**D**) UMAP plot of stromal cells, colored by cell type. The trajectory learned by Monocle3 is displayed. (**E**) Boxplots showing the fractional differences (Wilcoxon rank-sum test) of identified stromal subtypes between stress-high (red) and stress-low (blue) tumors. Each dot represents a tumor sample. All differences with FDR-adjusted $P < 0.05$ are indicated. (**F**) Scatter plot showing the correlation between the tumor compartment stress score and the stromal compartment CAF-2 scores in HERCULES cohort. Each dot represents a sample, colored by treatment phase. (**G**) Heatmaps and dot plots showing the activity (left), expression (middle), and regulatory potential (right) of the prioritized ligands in stressed cancer cells that drive the phenotype of the inflammatory stroma (CAF-2). (**H**) Heatmaps and dot plots showing the activity (left), expression (middle), and regulatory potential (right) of the prioritized ligands in inflammatory stroma (CAF-2) that drive the stress signature in the stressed cancer cells.

immunocompromised states within macrophages and CD8$^+$ T cells. The proinflammatory signaling molecules expressed by stress-associated cancer cells and iCAFs have the potential to promote paracrine feed-forward loops that can further induce these cell states. Targeting this signaling could be important, especially when chemotherapy is combined with immunotherapy, wherein ligands from iCAFs and stress-associated cancer cells may limit the chemotherapy-induced boost in the antitumor immune response. Our results of stress-associated cancer cells converge subclonal enrichment of cell state with feed-forward, immune suppressive paracrine signaling and offer both biomarkers and targets for novel combinatorial treatments.

DISCUSSION

Approximately half of the patients with HGSOC do not have HRD tumors and lack durable responses to either chemotherapy or PARP inhibitors, leading to short survival. To address this unmet clinical need, we characterized nongenetic mechanisms of chemoresistance in a poorly responding patient cohort. Our novel single-cell transcriptomics analysis approach on 22 paired treatment-naïve and post-NACT HGSOC specimens from 11 patients revealed a consistent increase in a stress-associated state upon treatment. This finding is in line with a smaller study performed with NanoString (40).

We independently validated the expression of the core stress response genes by RNA-ISH of matched nondissociated tissue sections, hence confirming that the signal we detect is not a dissociation artifact as seen in previous scRNA-seq studies (*27*, *41*). The stress-associated state distills core acute stress response by IEGs with inflammatory prosurvival signaling by NF-κB targets, as well as key regulators of EMT and stemness to protect cancer cells from chemotherapy. These cells resist apoptosis (*BCL6*) and can boost DNA repair via increased *ATF3*, which stabilizes the major DNA damage kinase ataxia telangiectasia mutated (*42*).

Our results showed that the proportion of proliferative cell population in treatment-naïve samples decreased from an average of 14% to an average of 3% in the post-NACT samples. Thus, we demonstrate that even in our poorly responding patient cohort, where the median PFI was 4.2 months and only three patients achieved response evaluation criteria in solid tumors (RECIST) complete response, chemotherapy has a fundamental impact on the phenotype of cancer cells. This implies that the chemoresistance mechanisms driving poor clinical response are not related to platinum uptake or efflux but rather to preexisting and induced cellular states.

We showed that chemotherapy reduces the low-stress subclones efficiently, at least partially due to the significantly reduced proliferation levels of low-stress subclones, leaving behind a higher proportion of the cells in subclones with initially increased transcriptomic stress response. The subclonal differences between treatment-naïve and post-NACT samples are not deterministic but rather slightly bias the cells toward the stress-associated state, analogous to what was shown for the cellular states of untreated glioblastoma specimens on the subclonal level (*16*). A previous analysis of paired pre- and post-NACT samples of triple-negative breast cancer found subclonal evolution to shape the genetic composition of tumors but failed to detect any shared definitive expression patterns to be subclonally enriched during chemotherapy (*13*). Thus, our results provide the first evidence of parallel subclonal selection of a defined transcriptional phenotype during chemotherapy in human tumors. Both the subclonal and patient level analyses strongly suggest that the preexisting stress-associated state primes the cancer cells to endure chemoresistance.

We did not detect recurrent genomic changes that would explain the subclonal differences in the stress-associated state, suggesting that they are either highly multigenic or based on epigenetic features or genomic aberrations other than CNAs. It remains to be assessed whether subclonal differences directly affect the level of intrinsic stress based on, for instance, metabolic features or rather modify the level of response to potential environmental stressors, such as hypoxia, lack of nutrition, or excess inflammatory signaling from their microenvironment.

Tumor stroma has been suggested to play a key role in chemoresistance of many cancers, including HGSOC, and increased tumor-stroma proportion at initial diagnosis of HGSOC associates with chemoresistance (*43*, *44*). Here, we found that, specifically, the *IL6* high iCAFs co-occur with the stress-associated cancer cells, complementing a recent spatial transcriptomics study of pancreatic ductal adenocarcinoma (*45*). A chemoresistant role for TME-derived interleukin-6 (IL6) is further supported by findings where increased IL6 in peritoneal fluid (*46*), ascites (*40*), or blood plasma (*47*) associate with worse prognosis of patients with HGSOC. Ligand-receptor analysis suggests that paracrine signaling is amplifying the stress response by a feed-forward loop in both cancer cells and iCAFs. This paracrine signaling is highly boosted by systemic platinum-taxane chemotherapy that not only causes extreme genotoxic and mitotic stress in cancer cells but also induces stress response in the nonproliferating stroma (*43*).

The stress-induced adaptation pattern we observed may offer avenues for therapeutic intervention. As direct targeting of the core immediate-early genes by mitogen-activated protein kinase/extracellular signal–regulated kinase pathway inhibitors is unlikely to work (*48*), targeting the inflammatory paracrine signaling may provide the most promising approach for combinatorial therapies. The nonproliferating TME is not under selective evolutionary pressure, reducing the risk of treatment resistance. Among the current treatment regimens, the antiangiogenic bevacizumab may hold promise for the *IL6*-expressing stress-high tumors, as increased plasma levels of IL6 are indicative of bevacizumab sensitivity in HGSOC (*47*). Furthermore, antibodies against IL6, TNF, LIF, CXCL12, or their receptors, some of which are already in clinical use to treat inflammatory diseases, have shown initially promising results in preclinical models when combined with platinum chemotherapy (*49*–*52*). In addition, the regulators up- and downstream of *IL6*, namely, *STAT3* and Toll-like receptors, respectively, have been successfully targeted in resistant cancer models (*53*, *54*). Targeting these inflammatory cytokines has also shown promising results in combination with immunotherapies [e.g., in ovarian cancer models (*55*, *56*)] This implies that the stress response may provide cancer cells with resistance against a wide array of treatments, from chemotherapy to targeted therapies and immunotherapies, and thus provide targets for a generalized strategy to oppose resistance in cancer.

We have identified a stress-associated state that distills acute stress response with paracrine inflammatory signaling to provide cancer cells with adaptation, promoting chemoresistance on both subclone and patient level. Overall, our results support a combination of induced and selective processes to explain chemotherapy-induced transcriptomic changes as suggested in (*13*), modified by both subtle genetic differences and changes in the TME signals. Furthermore, the identification of stress signature opens avenues for combinatorial drug testing in preclinical models that maintain both subclonal heterogeneity and paracrine tumor-stromal signaling. As many drugs targeting inflammatory effectors are already in clinical use for other indications, they may offer a realistic option for safe combinatorial therapies with a wide array of currently used oncological drugs to restrain the broadly adaptive stress response of tumors.

MATERIALS AND METHODS

Human participants

All patients participating in the study provided written informed consent. The study and the use of all clinical materials have been approved by the Ethics Committee of the Hospital District of Southwest Finland (ETMK) under decision number EMTK: 145/1801/2015.

The clinical specimens used in the study represent several understudied aspects of HGSOC that are poorly represented in existing cohorts of clinical specimens, such as TCGA (*5*). Contrary to TCGA data, all our paired samples were collected from intra-abdominal, peritoneal, and omental metastases, thus representing cancer cell populations with proven metastatic potential. The material was from solid tumors, containing potentially chemoprotective stromal TME, which is missing from the more broadly available ascites samples. Our cohort also included low purity tumors that may represent a distinct, poor prognosis phenotype of HGSOC, which are missing from most genomic analyses.

scRNA-seq sample preparation

Prospective HGSOC tumor specimens were collected from 11 patients at the time of laparoscopy and IDS. Detailed clinical information is shown in Table 1. Immediately after surgery, the specimens were incubated overnight in a mixture of collagenase and hyaluronidase (Department of Pathology, University of Turku) to obtain single-cell suspensions. For samples specified in Table 1, single-cell suspensions were frozen in STEM-CELLBANKER DMSO-FREE solution (#11897F, AMSBIO) and thawed in culture medium immediately before processing for scRNA-seq. The viability of the frozen single-cell suspensions ranged from 65 to 94% after thawing, with a median of 80%. scRNA-seq libraries were prepared with the Chromium Single-Cell 3′ Reagent Kit v. 2.0 (10x Genomics) and sequenced on Illumina HiSeq 4000 (Jussi Taipale Lab, Karolinska Institute, Sweden), HiSeq 2500, and NovaSeq 6000 instruments (Sequencing Unit of the Institute for Molecular Medicine Finland, Finland).

Preprocessing scRNA-seq data

The Cell Ranger software suite (version 3.1.0) was used to perform sample demultiplexing, alignment, barcode processing, and UMI quantification. The reference index was built upon the GRCh38.d1.vd1 reference genome with GENCODE v25 annotation. We applied a three-step filtering approach to filter out low-quality cells. In the first steps, we excluded cells expressing any combinations of *PAX8*, *DCN*, and *PTPRC* to remove potential doublets and removed cells with above 15% UMI counts originating from mitochondrial genes. Then, we used the shared nearest neighbor (SNN) modularity optimization–based clustering from Seurat v3 (*15*) for initial clustering. Three major cell types were revealed on the basis of acknowledged markers: epithelial cancer cells (*WFDC2*, *PAX8*, and *EPCAM*), stromal cells (*COL1A2*, *FGFR1*, and *DCN*), and immune cells (*CD79A*, *FCER1G*, and *PTPRC*).

In the second filtering step, we quantified the quality measures of each cell using Seurat v3 (*15*). We estimated the cutoffs for each quality measure in each cell type based on its bimodal distribution (fig. S1B) and then used four criteria for quality control: (i) the number of reads above 8192 for cancer cell, 4096 for stromal cells, and 2896 for immune cells; (ii) the number of UMI counts above 4075 for cancer cells, 2048 for stromal cells, and 1024 for immune cells; (iii) the number of detected genes above 1552 for cancer cells, 1024 for stromal cells, and 512 for immune cells; and (iv) the percentage of UMI counts originating from mitochondrial genes below 12 for cancer cells and 7.5 for stromal and immune cells. Third, we filtered out epithelial cells with inferred CNA profiles that clustered together with stromal cells.

Modeling and clustering scRNA-seq data of cancer cells using PRIMUS

PRIMUS models the observed single-cell expression profiles as a mixture of latent phenotypic transcriptional profiles and nuisance expression profiles following a Poisson distribution

$$Y_{j,i} \sim \text{Poisson}\left(\left(\sum_{l=1}^{r}(X_{j,l}D_{l,i})+\sum_{c=1}^{k}(Z_{j,c}C_{c,i})\right)G_i\right) \qquad (1)$$

where $l = 1,2, \ldots, r$ runs over the r nuisance factors and $c = 1,2, \ldots, k$ runs over k latent phenotypic clusters. $Y_{j,i}$ denotes the observed UMI counts of gene j in the ith cell, $X_{j,l}$ denotes the expression profile centroid of gene j specific to nuisance factor l, $D_{l,i}$ denotes the design coefficient of the lth nuisance factor in the ith cell, $Z_{j,c}$ denotes the cluster c expression profile centroid at gene j, $C_{c,i} \in \{0,1\}$ is an indicator of whether the ith cell belongs to the cluster c, and G_i is a cell-specific scaling factor.

A linear model, such as in Eq. 1, is appropriate when the action of nuisance signals and the biological phenotypic signals can be considered additive. This occurs when the processes are parallel or their action is nonoverlapping, e.g., when specific pathways (or the genes within) are controlled by the patient-specific component and others are controlled by the cell state. The use of a stochastic model permits natural variation between cells.

We highlight that while the underlying components are Poissonian, the observed counts $Y_{j,i}$ is a mixture of Poisson-distributed factors with unequal rates, as specific in Eq. 1, which results in an overdispersed data distribution. The Poisson model is also well suited for capturing random RNA dropout (*57*, *58*), which is commonly observed in scRNA-seq data (*59*).

Given the observations $Y_{j,i}$, known nuisances $D_{l,\,i}$, known scaling factors G_i, and the number of latent clusters k, we can estimate the latent nuisance expression centroids $X_{j,l}$, latent expression centroids $Z_{j,c}$, and the latent cluster memberships $C_{c,i}$ using an expectation-maximization (EM) algorithm (*60*). The EM algorithm is constructed on the latent variables $Z_{X_{j,l,i}} \sim \text{Poisson}(X_{j,l}D_{l,i}G_i)$ and $Z_{Zj,c,i} \sim \text{Poisson}(Z_{j,c}C_{c,i}G_i)$, which are the nuisance and cleaned contributions to the expression, respectively. The parameter set $\theta = (X_{j,l}, Z_{j,c}, C_{c,i})$ was estimated in two stages: First, the expression centroids $X_{j,l}$ and $Z_{j,c}$ can be estimated given $Y_{j,i}$, $D_{l,i}$, $C_{c,i}$, and G_i; second, the cluster membership $C_{c,i}$ can be updated given $Y_{j,i}$, $X_{j,l}$, $D_{l,i}$, $Z_{j,c}$, and G_i. Given $Y_{j,i}$, $D_{l,i}$, G_i, and the estimated $X_{j,l}$, we further computed $\widetilde{Z}_{j,i}$, the denoised expression of gene j in the ith cell by solving $Y_{j,i} \sim \text{Poisson}\,((\sum_{l=1}^{r}(X_{j,l}D_{l,i})+\widetilde{Z}_{j,i})\,G_i)$ for $\widetilde{Z}_{j,i}$. See the Supplementary Materials for details.

To select the optimal k, we fitted PRIMUS for $k = 1,2, \ldots,25$ with 10 different random initial parameter sets for each k, and $k = 12$ was selected on the basis of BIC (fig. S2A). We then ran the EM procedure with 200 random initializations for $k = 12$, the maximum likelihood estimates of $X_{j,l}$ and $Z_{j,c}$, and $C_{c,i}$ and $\widetilde{Z}_{j,i}$ were used for downstream analysis. The model selection process also acts as a regularizer for penalizing clusters that are solely correlating with the modeled nuisance factors. This tends to make the method to favor solutions where the effect of the confounding factors is completely eliminated in case of overlap.

Simulation of scRNA-seq datasets

We simulated scRNA-seq datasets using the splatPop model from the R package splatter (*24*, *25*). Provided with genotype information for a population, splatPop models expression quantitative trait loci (eQTL) effects and simulates gene counts for single cells for individuals in the population. Following the suggested pipeline (https://bioconductor.org/packages/release/bioc/vignettes/splatter/inst/doc/splatPop.html), we used the mockVCF function to generate mock variant call format (vcf) files for 20,000 single-nucleotide polymorphisms in six samples, the mockBulkeQTL function to generated mock eQTL mapping results for 5000 genes, and the mockBulkMatrix function to generate mock bulk expression data of 5000 genes for a population with 100 samples, with the default parameters. We next estimated the simulation parameters for the eQTL population simulation from the generated mock eQTL mapping results and bulk expression data using the splatPopEstimate function. Last, we used the splatPopSimulate function to simulate scRNA-seq count data using the mock vcf files and the estimated parameters for six samples and five cell groups under three scenarios (table S1): (i) All six samples contain the five cell groups (3000 cells and 5000 genes); (ii) each sample only contains a subset of cell groups, three pairs of samples had no cell types in common, and there was one sample-specific cell group (1400 cells and 5000 genes); (iii) the same setting with scenario ii but with unbalanced cell numbers in each sample (from 20 to 2000). We simulated 20 random datasets from each scenario for benchmarking.

Human pancreatic datasets

We obtained five human pancreatic datasets and the corresponding cell type annotations from https://github.com/JinmiaoChenLab/Batch-effect-removal-benchmarking/tree/master/Data/dataset4 (*61*). This dataset contains 14,767 cells in total with 15,558 genes for 15 different cell types and 45 samples from five studies (*62–66*). The sample labels were collected from GSE84133 (*62*), GSE85241 (*63*), E-MTAB-5061 (*64*), GSE83139 (*65*), and GSE81608 (*66*), respectively. We randomly sampled 80% of the cells 20 times and assessed the cell type identification performance of PRIMUS and other methods on the subsampled datasets.

Comparison of PRIMUS to other methods

We compared PRIMUS to five commonly used single-cell data integration methods [Seurat v3 (*15*), Harmony (*19*), LIGER (*18*), mnnCorrect (*23*), and fastMNN (*23*)] and three bulk data integration methods [ComBat (*21*), ComBat-seq (*22*), and limma (*20*)].

PRIMUS

PRIMUS takes the raw count matrix, design of nuisance factors, and scaling factors as inputs. For the simulated datasets, the nuisance factors were the sample labels, and the scaling factors were estimated using the logNormCounts function from scater R package (version 1.20.0) (*67*) following the splatPop (*24*, *25*) simulation tutorial. For the pancreatic datasets, the nuisance factors were the sample labels, and the scaling factors were estimated using the prism-gain function from the PRISM package (*31*). The number of clusters *k* was set to the same as the number of cell groups/types, and the maximum number of iterations for EM procedure was set to 200.

Seurat v3

We ran Seurat v3.2.3 (*15*) as described in Seurat's integration tutorial (https://satijalab.org/seurat/articles/integration_introduction.html) for the pancreatic datasets and simulation scenarios i and ii datasets. Sample_6 in scenario iii contained only 20 cells, and sample ICRH76 from the pancreatic datasets contains only 19 cells, which were too few for Seurat v3 to perform integration, so Seurat v3 was not run on datasets from scenario iii and the pancreatic datasets. We performed clustering on the first 30 principal components (PCs) for the integrated pancreatic datasets and on the first 20 PCs for the integrated simulated datasets, using the FindNeighbors and FindClusters functions.

Harmony

We ran Harmony (*19*) according to its online tutorial (https://github.com/immunogenomics/harmony). We ran Harmony with default parameters on the first 30 PCs for the pancreatic datasets and the first 20 PCs for the simulated datasets and obtained the corrected PC embeddings. We used FindNeighbors and FindClusters functions from Seurat v3 (*15*) to run clustering on Harmony-corrected PC embeddings.

LIGER

We ran LIGER (rliger package, version 1.0.0) (*18*) with the default parameters ($k = 20, \lambda = 5$) as suggested in the integration tutorial (http://htmlpreview.github.io/?https://github.com/welch-lab/liger/blob/master/vignettes/Integrating_multi_scRNA_data.html). We set $k = 10$ for the pancreatic datasets as the smallest sample contains only 19 cells.

mnnCorrect and fastMNN

We followed the tutorial (http://bioconductor.org/packages/devel/bioc/vignettes/batchelor/inst/doc/correction.html) to run the mnnCorrect and the fastMNN functions from the batchelor package (version 1.8.0) (*23*). We used the top 5000 and top 1000 highly variable genes (HVGs) for correction for the pancreatic datasets and the simulated datasets, respectively. All other parameters were kept as default values.

ComBat and ComBat-seq

ComBat (*21*) was initially designed to remove batch effects in microarray data, and ComBat-seq (*22*) is an extension of ComBat to address batch effects in bulk RNA-seq data. We ran ComBat and ComBat-seq using the implementation in the R package sva (version 3.40.0) (*68*) with default parameters.

limma

We followed the user guide https://www.bioconductor.org/packages/devel/bioc/vignettes/limma/inst/doc/usersguide.pdf to run limma (version 3.50.0) (20). As limma expects normalized and log-transformed data as input, we first normalized the raw counts using the "LogNormalize" method from the NormalizeData function in Seurat v3 (*15*) and ran limma with the normalized data using the removeBatchEffect with default parameters.

For mnnCorrect, fastMNN, ComBat, ComBat-seq, and limma, which do not have recommended clustering approaches in their online tutorials, we applied the Louvain clustering (*69*) implemented in LIGER (*18*) on their integration outputs. For all methods except for PRIMUS, the clustering was run with the resolution parameter ranging from 0.01 to 5, and the outputs with the number of clusters the same as the number of cell groups/types were used.

We computed the adjusted rand index (ARI) (*70*) to compare the cell group/type labels with the computed cluster labels for the simulated and pancreatic datasets. We used the adjustedRandIndex from the mclust R package (version 5.4.7) (*71*) to compute ARI.

Differential expression analysis for cancer cells

We used an LRT to perform the differential expression (DE) analysis controlling for the nuisance factors. Let $Y_{j,\,i}$ denote the observed UMI count of gene *j* in the *i*th cell, $\mu_{j,i} = \left(\sum_{l=1}^{r}(X_{j,l}D_{l,i}) + \sum_{c=1}^{k}(Z_{j,c}C_{c,i})\right)G_i$ denotes the predicted mean expression rate of gene *j* for the *i*th cell based on the estimated model parameters $X_{j,l}$, $Z_{j,c}$, and $C_{c,i}$. The DE between group g_1 and group g_2 for the gene *j* can be assessed by testing the alternative hypothesis $H_A : Z_{j,g1} \neq Z_{j,g2}$ against the null hypothesis $H_0 : Z_{j,g1} = Z_{j,g2}$. For the former, the likelihood is that attained at the maximum-likelihood estimate (MLE) $\hat{\mu}_{j,i}$, while for the latter, the model is refitted giving $\bar{\mu}_{j,i}$, the MLE under H_0. The logarithmic LRT statistic for gene *j* is

$$\mathrm{LRT}_j = \sum_{i \in I_1 \cup I_2}(Y_{j,i}\log\hat{\mu}_{j,i} - \hat{\mu}_{j,i}) - \sum_{i \in I_1 \cup I_2}(Y_{j,i}\log\bar{\mu}_{j,i} - \bar{\mu}_{j,i})$$

where $I_1$and I_2 denote the indices for the samples in $g_1$and g_2, respectively. A *P* value for the gene *j* to be differentially expressed between group g_1 and group g_2 can be computed as the probability to the right of the $-2\mathrm{LRT}_j$ for the chi-squared distribution with degrees of freedom is equal to the difference in number of parameters, i.e., 1.

Identification of coexpressed gene communities

Coexpressed gene communities were identified as follows: (i) We conducted DE analysis between each pair of cell clusters, resulting in 66 comparisons. The top 1000 most significant LRT genes with an FDR of <0.01 were selected in each comparison, and this resulted in a total of 4742 genes; (ii) the Pearson correlations between these 4742 genes were computed using the LRTs from all 66 comparisons. Correlations with $\rho > 0.8$ and $P < 0.01$ were used to build a gene network; (iii) we detected 916 communities in the network using the Walktrap community finding algorithm with step equals to 3 (*72*), and the 10 communities consisting of more than 30 genes were retained for further analysis; (iv) let V be the genes in a community, c_j be the coreness of gene j, and $n_{\max}$ be the number of genes with the maximum coreness ($\max_{j \in V} c_j$, degeneracy) in that community. If $n_{\max} > 30$, then the genes with $c_j = \max_{j \in V} c_j$ were retained; otherwise, we retained the top 30 genes ranked by coreness; (v) gene set overrepresentation analysis was performed for the remaining genes in each community using the ConsensusPathDB (*26*). We further reduced the redundancy of each gene community with number of genes above 20 by applying the following filters: (i) Only genes overlapped with significantly overrepresented gene sets (FDR < 0.05, size <500) were kept; and (ii) biclustering was applied on the binary matrix of the presence/absence of each gene in each significantly overrepresented gene set using the R package blockcluster (version 4.4.3) (*73*), and the gene clusters that have less than 3% presence in any of the gene set clusters were excluded. After filtering, the numbers of genes per community were between 11 and 106. The genes in each community are listed in table S2.

Quantification of stress scores and proliferation scores from RNA-seq data

We defined the stress score as the gene set enrichment score of our identified stress-associated gene signature in individual cells and samples, which was computed using Single sample Gene Set Enrichment analysis (ssGSEA) (*74*). Samples with permutation test P value below 0.05 by permutation test were considered stress-high, while samples with P value above 0.5 were considered stress-low.

Similarly, we quantified the proliferation score as the gene set enrichment score of the proliferative DNA repair gene signature in individual cells and samples using ssGSEA (*74*).

RNA-ISH and imaging

RNA-ISH was performed on fresh 3-μm formalin-fixed paraffin-embedded tissue sections using the RNAscope Multiplex Fluorescent Reagent Kit version 2 for target detection (#323100, Advanced Cell Diagnostics) according to the manual. Briefly, tissue sections were baked for 1 hour at 60°C, then deparaffinized, and treated with hydrogen peroxide for 10 min at room temperature. Target retrieval was performed for 15 min at 98°C, followed by protease plus treatment for 15 min at 40°C. All RNAscope probes (tables S3 and S4) were hybridized for 2 hours at 40°C, followed by signal amplification, and development of horseradish peroxidase channels was performed according to the manual. TSA Plus fluorophores fluorescein (1:750 dilution), Cyanine 3 (1:1500 dilution), and Cyanine 5 (1:3000 dilution) (NEL744001KT, PerkinElmer) were used for signal detection. The sections were counterstained with 4′,6-diamidino-2-phenylindole (DAPI) and mounted with the ProLong Gold Antifade Mountant (P36930, Invitrogen). Images were generated using 3DHISTECH Pannoramic 250 Flash II digital slide scanner at the Genome Biology Unit supported by HiLIFE and the Faculty of Medicine, University of Helsinki, and Biocenter Finland. All samples were scanned using ×40 magnification with extended focus and seven focus levels.

Quantitative analysis of whole-slide RNA-ISH images

We used CaseViewer (version 2.3.0, 3DHISTECH Ltd.) to read the MRXS immunofluorescence image and to separate its different channels into the DAPI staining, and fluorescein (FITC 38 HE), Cyanine 3 (TRITC 48 HE) and Cyanine 5 (Cy5) channels for gene expression quantification. CellProfiler (version 3.1.8) (*75*) was used for segmentation in the DAPI staining. The nondefault parameters that were determined experimentally were as follows: A typical diameter of 18 to 56 pixels, thresholding using adaptive Otsu's method, clumped object detection and splitting using shape, and low-resolution speedups were disabled. The segmented objects were classified into cancer, immune, and stromal cells using the DAPI staining and its segmentation. For this, we extracted the area, the mean nucleus stain intensity, and the eccentricity of each segmented object. Subsequently, we trained a supervised quadratic classifier using different training sets of cells with the properties mentioned above and desired cell types. Since the cancer and immune cell morphology and intensity change from primary to interval samples and there are also some stromal cells hard to distinguish from small cancer cells, we trained multiple classifiers to obtain the highest classification accuracy per image. The classification results were visually assessed by a pathologist. Afterward, the classifier was used to predict the cell types using the computed features in untrained images. The quadratic classifier was implemented in MATLAB (version R2019b) and was trained with uniform class priors. We extracted spatial probability maps for each cell type from the quadratic classifier, which were then low pass–filtered in logarithmic space (probability product space) using a disk kernel of 100-pixel radius (cf. cell radius of ~20). This propagates the probability of classification to neighboring cells in the regions with large classification uncertainty, but for a cell exhibiting strong features of a particular type, its class will be unaffected.

Since some RNA signals are localized in the cytoplasm of the cells, we have expanded the segments of corresponding tumor, immune, and stromal nuclei to include the cellular cytoplasm. This expansion was performed by dilating the segments in the unlabeled space with a disk kernel with a radius size of 20, 5, and 5 pixels for the tumor, immune, and stromal classes, respectively. Ties were broken to the nearest segment. The parameters were tuned experimentally to account for the different sizes between the different cell types.

We reduced the cross-channel fluorescence bleed of Cy5, FITC, and TRITC staining by finding a suitable basis for the intensity data near the principal axes using power iteration. The fluorescence intensity signal was quantified using the negative response of a Laplacian of Gaussian filter with standard deviation of unity. The value was tuned manually, and the kernel width roughly corresponds to the diameter of an observed RNA spot in our images. This procedure filters out background variations and cellular autofluorescence, leaving intensity blobs of the specified size.

Quantification of stress score from RNA-ISH data

To quantify the stress score using expression levels of the 10 stress-associated genes measured with RNA-ISH experiment, we performed the CCA between the RNA-ISH expression levels and the combination of treatment phase information and the scRNA-seq–derived stress score. The resulting first canonical component of the RNA-ISH quantifications, which is a linear combination of the expression levels of the 10 genes, was defined as the "RNA-ISH stress score." The coefficients for each gene in the first canonical component of the RNA-ISH data are given in table S5.

To assess the significance of the correlation between the RNA-ISH and scRNA-seq stress scores and the difference between the treatment-naïve/post-NACT pairs in RNA-ISH stress scores, each of which is expected to have nonzero correlation by construction, the data were permuted 10^5 times, and the analysis was applied on the permuted datasets to obtain empirical P values.

Inference of CNA and clonal structure

The CNAs and subclones were inferred using inferCNV (version 1.4.0) (*30*) with the following parameters: "cutoff=0.1, denoise=TRUE, HMM=TRUE, hclust_method='ward.D2', tumor_subcluster_partition_method='random_trees', tumor_subcluster_pval=0.05, num_threads = 10." We randomly sampled up to 150 stromal cells from each patient to serve as reference. We filtered out the subclones with less than five cells. The phylogenetic trees were generated using UPhyloplot2 (*76*).

TME cell type annotation

Clustering of stromal and immune cells was performed using Seurat v3 (*15*). We selected the top 3000 HVGs using the FindVariableFeatures function with the method "vst." The expression of those HVGs was centered and scaled using the ScaleData function with default parameters. We performed PC analysis on the scaled data, and the SNN modularity optimization–based clustering was conducted using the first 50 PCs with a resolution parameter of 3. Next, we performed cell type annotation using Scibet (*77*), a supervised cell type annotation tool, which can accurately predict cell identities regardless of technical factors or batch effect (*77*), as follows: (i) First, we predicted the cell type for each stromal and immune cell with a trained model provided by Scibet, which includes 30 major human cell types from 42 scRNA-seq datasets as the reference. (ii) Second, for each cell type identified in step i, we used the cells from the clusters, of which more than 75% cells belong to that cell type, to build a new reference set. (iii) Third, we annotated the remaining cells using SciBet with the reference set built in step ii. The cell type name was corrected manually in accordance with known gene markers: B cells (*CD79A*$^+$ and *MS4A1*$^+$), DC-1 (*CLEC10A*$^+$, *FCER1A*$^+$, and *CD1C*$^+$), DC-2 (*LAMP*$^+$), ILCs (*TNFRSF18*$^+$ and *TNFRSF25*$^+$), macrophages (*FCER1G*$^+$), mast cells (*TPSAB1*$^+$), NK cells (*KLRB1*$^+$ and *KLRD1*$^+$), plasmacytoid DCs (*GZMB*$^+$), plasma cells (*MZB1*$^+$), T cells (*CD3D*$^+$), endothelial cells (*PECAM1*$^+$ and *THBD*$^+$), and mesothelial cells (*KRT8*$^+$ and *KRT19*$^+$). We identified CAFs as cell clusters that are positive for *FAP* and negative for cytokeratins (*KRT8*, *KRT18*, and *KRT19*). CAF subtypes were annotated on the basis of the markers: CAF-1 (*MMP1*$^+$ and *MMP9*$^+$), CAF-2 (*LIF*$^+$, *IL6*$^+$, *CXCL12*$^+$, and *CFD*$^+$), and CAF-3 (*ACTA2*$^+$ and *MYL9*$^+$).

Trajectory analysis of stromal cells

To explore the relations of the identified stromal cell types, we constructed the cell trajectories using Monocle3 (version 1.0.0) (*78*). We removed the sample-specific variations and the effect of the percentage of the UMI counts originating from mitochondrial genes using PRIMUS before applying Monocle3. The denoised counts were log-transformed and projected into the first 30 PCs. We then computed the uniform manifold approximation and projection (UMAP) using the reduce_dimension function from Monocle3 with cosine distance, and the minimum distance was set to 0.3. We clustered the cells using the cluster_cells function with default parameters. Last, Monocle3 learned the trajectory graph using the learn_graph function with default parameters.

DE analysis for TME cells

The identification of CAF subtype marker genes and the DE analysis between stress-high and stress-low samples for TME cells were conducted using the Seurat v3 (*15*) function FindMarkers using the negbinom test with the UMI counts, patient labels, library preparation method, and sequencing instruments as the latent variables.

NicheNet analysis

NicheNet (*79*) was used to explore the cell to cell interactions between stressed cancer cells and iCAFs. We first calculated two sets of DEGs: CAF-2 versus CAF-1 and CAF-2 [DEG set1; $\log_2$ fold change ($\log_2$FC) > 0.25, adjusted $P < 0.01$, expressed in at least 25% of iCAFs] and stressed cancer cells versus other cancer cells (DEG set2; $\log_2$FC > 1, adjusted $P < 0.01$, expressed in at least 25% of stressed cancer cells). To identify which ligands produced by stressed cancer cells are driving the phenotype of CAF-2, we used the top 200 up-regulated genes in DEG set1 based on adjusted P value as gene set of interest. All genes expressed in at least 25% of CAF-2 were used as a background gene set. We required the potential ligands to be higher expressed in stressed cancer cells compared to other cancer cells (DEG set2) to narrow down the number of ligands to be evaluated. Similarly, we also identified the potential ligands produced by CAF-2 that are active in driving the stress signature in stressed cancer cells. The 35 genes in the stress signature were defined as the gene set of interest, and the background gene set included all genes expressed in at least 25% of stressed cancer cells. The potential ligands were higher expressed in CAF-2 compared to other CAFs (DEG set1). The lists of the DEG sets used in this analysis are provided in data S1 and S2.

Bulk tumor expression data

We acquired 18 treatment-naïve versus post-NACT sample pairs and 8 primary-relapse sample pairs from 23 patients in the HERCULES cohort (http://project-hercules.eu/). The sample collection, data quality control, alignment, and quantification were performed as we have previously described (*31*).

TCGA RNA-seq data of ovarian serous cystadenocarcinoma (OV, illuminahiseq_rnaseqv2-RSEM_genes_normalized) was downloaded from the Broad Firehose (https://gdac.broadinstitute.org/), along with the clinical annotations. The primary tumors from 271 patients with advanced HGSOC (grade: G2 to G4, stage: IIIA to IV) and with PFS data available were included in our analysis. The proportions of tumor, stromal, and immune components and the cell type–specific expression profiles for HERCULES and TCGA samples were estimated using PRISM (*31*).

TCGA reverse phase protein array data

The reverse phase protein array data (replicates-based normalization) for TCGA ovarian serous cystadenocarcinoma samples (TCGA-OV-L4) was downloaded from the Cancer Proteomics Atlas (https://tcpaportal.org/tcpa/download.html).

SUPPLEMENTARY MATERIALS

Supplementary material for this article is available at https://science.org/doi/10.1126/sciadv.abm1831

View/request a protocol for this paper from *Bio-protocol*.

REFERENCES AND NOTES

1. L. Kelland, The resurgence of platinum-based cancer chemotherapy. *Nat. Rev. Cancer* **7**, 573–584 (2007).
2. J. P. Neijt, W. W. ten Bokkel Huinink, M. E. van der Burg, A. T. van Oosterom, P. H. Willemse, J. B. Vermorken, A. C. van Lindert, A. P. Heintz, E. Aartsen, M. van Lent, Long-term survival in ovarian cancer. *Eur. J. Cancer.* **27**, 1367–1372 (1991).
3. L. A. Torre, B. Trabert, C. E. DeSantis, K. D. Miller, G. Samimi, C. D. Runowicz, M. M. Gaudet, A. Jemal, R. L. Siegel, Ovarian cancer statistics, 2018. *CA Cancer J. Clin.* **68**, 284–296 (2018).
4. A. A. Ahmed, D. Etemadmoghadam, J. Temple, A. G. Lynch, M. Riad, R. Sharma, C. Stewart, S. Fereday, C. Caldas, A. Defazio, D. Bowtell, J. D. Brenton, Driver mutations in TP53 are ubiquitous in high grade serous carcinoma of the ovary. *J. Pathol.* **221**, 49–56 (2010).
5. D. Bell, A. Berchuck, M. Birrer, J. Chien, D. W. Cramer, F. Dao, R. Dhir, P. DiSaia, H. Gabra, P. Glenn, A. K. Godwin, J. Gross, L. Hartmann, M. Huang, D. G. Huntsman, M. Iacocca, M. Imielinski, S. Kalloger, B. Y. Karlan, D. A. Levine, G. B. Mills, C. Morrison, D. Mutch, N. Olvera, S. Orsulic, K. Park, N. Petrelli, B. Rabeno, J. S. Rader, B. I. Sikic, K. Smith-McCune, A. K. Sood, D. Bowtell, R. Penny, J. R. Testa, Integrated genomic analyses of ovarian carcinoma. *Nature* **474**, 609–615 (2011).
6. M. R. Mirza, R. L. Coleman, A. González-Martín, K. N. Moore, N. Colombo, I. Ray-Coquard, S. Pignata, The forefront of ovarian cancer therapy: Update on PARP inhibitors. *Ann. Oncol.* **31**, 1148–1159 (2020).
7. N. C. Turner, J. S. Reis-Filho, Genetic heterogeneity and cancer drug resistance. *Lancet Oncol.* **13**, e178–e185 (2012).
8. M. Gerlinger, A. J. Rowan, S. Horswell, M. Math, J. Larkin, D. Endesfelder, E. Gronroos, P. Martinez, N. Matthews, A. Stewart, P. Tarpey, I. Varela, B. Phillimore, S. Begum, N. Q. McDonald, A. Butler, D. Jones, K. Raine, C. Latimer, C. R. Santos, M. Nohadani, A. C. Eklund, B. Spencer-Dene, G. Clark, L. Pickering, G. Stamp, M. Gore, Z. Szallasi, J. Downward, P. A. Futreal, C. Swanton, Intratumor heterogeneity and branched evolution revealed by multiregion sequencing. *N. Engl. J. Med.* **366**, 883–892 (2012).
9. A. B. Turke, K. Zejnullahu, Y.-L. Wu, Y. Song, D. Dias-Santagata, E. Lifshits, L. Toschi, A. Rogers, T. Mok, L. Sequist, N. I. Lindeman, C. Murphy, S. Akhavanfard, B. Y. Yeap, Y. Xiao, M. Capelletti, A. J. Iafrate, C. Lee, J. G. Christensen, J. A. Engelman, P. A. Jänne, Preexistence and clonal selection of MET amplification in EGFR mutant NSCLC. *Cancer Cell* **17**, 77–88 (2010).
10. B. Norquist, K. A. Wurz, C. C. Pennil, R. Garcia, J. Gross, W. Sakai, B. Y. Karlan, T. Taniguchi, E. M. Swisher, Secondary somatic mutations restoring BRCA1/2 predict chemotherapy resistance in hereditary ovarian carcinomas. *J. Clin. Oncol.* **29**, 3008–3015 (2011).
11. O. Pich, F. Muiños, M. P. Lolkema, N. Steeghs, A. Gonzalez-Perez, N. Lopez-Bigas, The mutational footprints of cancer therapies. *Nat. Genet.* **51**, 1732–1740 (2019).
12. L. Galluzzi, L. Senovilla, I. Vitale, J. Michels, I. Martins, O. Kepp, M. Castedo, G. Kroemer, Molecular mechanisms of cisplatin resistance. *Oncogene* **31**, 1869–1883 (2012).
13. C. Kim, R. Gao, E. Sei, R. Brandt, J. Hartman, T. Hatschek, N. Crosetto, T. Foukakis, N. E. Navin, Chemoresistance evolution in triple-negative breast cancer delineated by single-cell sequencing. *Cell* **173**, 879–893.e13 (2018).
14. A. Maynard, C. E. McCoach, J. K. Rotow, L. Harris, F. Haderk, D. L. Kerr, E. A. Yu, E. L. Schenk, W. Tan, A. Zee, M. Tan, P. Gui, T. Lea, W. Wu, A. Urisman, K. Jones, R. Sit, P. K. Kolli, E. Seeley, Y. Gesthalter, D. D. Le, K. A. Yamauchi, D. M. Naeger, S. Bandyopadhyay, K. Shah, L. Cech, N. J. Thomas, A. Gupta, M. Gonzalez, H. Do, L. Tan, B. Bacaltos, R. Gomez-Sjoberg, M. Gubens, T. Jahan, J. R. Kratz, D. Jablons, N. Neff, R. C. Doebele, J. Weissman, C. M. Blakely, S. Darmanis, T. G. Bivona, Therapy-induced evolution of human lung cancer revealed by single-cell RNA sequencing. *Cell* **182**, 1232–1251.e22 (2020).
15. T. Stuart, A. Butler, P. Hoffman, C. Hafemeister, E. Papalexi, W. M. Mauck III, Y. Hao, M. Stoeckius, P. Smibert, R. Satija, Comprehensive integration of single-cell data. *Cell* **177**, 1888–1902.e21 (2019).
16. C. Neftel, J. Laffy, M. G. Filbin, T. Hara, M. E. Shore, G. J. Rahme, A. R. Richman, D. Silverbush, M. L. Shaw, C. M. Hebert, J. Dewitt, S. Gritsch, E. M. Perez, L. N. G. Castro, X. Lan, N. Druck, C. Rodman, D. Dionne, A. Kaplan, M. S. Bertalan, J. Small, K. Pelton, S. Becker, D. Bonal, Q.-D. Nguyen, R. L. Servis, J. M. Fung, R. Mylvaganam, L. Mayr, J. Gojo, C. Haberler, R. Geyeregger, T. Czech, I. Slavc, B. V. Nahed, W. T. Curry, B. S. Carter, H. Wakimoto, P. K. Brastianos, T. T. Batchelor, A. Stemmer-Rachamimov, M. Martinez-Lage, M. P. Frosch, I. Stamenkovic, N. Riggi, E. Rheinbay, M. Monje, O. Rozenblatt-Rosen, D. P. Cahill, A. P. Patel, T. Hunter, I. M. Verma, K. L. Ligon, D. N. Louis, A. Regev, B. E. Bernstein, I. Tirosh, M. L. Suvà, An integrative model of cellular states, plasticity, and genetics for glioblastoma. *Cell* **178**, 835–849.e21 (2019).
17. S. V. Puram, I. Tirosh, A. S. Parikh, A. P. Patel, K. Yizhak, S. Gillespie, C. Rodman, C. L. Luo, E. A. Mroz, K. S. Emerick, D. G. Deschler, M. A. Varvares, R. Mylvaganam, O. Rozenblatt-Rosen, J. W. Rocco, W. C. Faquin, D. T. Lin, A. Regev, B. E. Bernstein, Single-cell transcriptomic analysis of primary and metastatic tumor ecosystems in head and neck cancer. *Cell* **171**, 1611–1624.e24 (2017).
18. J. D. Welch, V. Kozareva, A. Ferreira, C. Vanderburg, C. Martin, E. Z. Macosko, Single-cell multi-omic integration compares and contrasts features of brain cell identity. *Cell* **177**, 1873–1887.e17 (2019).
19. I. Korsunsky, N. Millard, J. Fan, K. Slowikowski, F. Zhang, K. Wei, Y. Baglaenko, M. Brenner, P.-R. Loh, S. Raychaudhuri, Fast, sensitive and accurate integration of single-cell data with harmony. *Nat. Methods* **16**, 1289–1296 (2019).
20. M. E. Ritchie, B. Phipson, D. Wu, Y. Hu, C. W. Law, W. Shi, G. K. Smyth, limma powers differential expression analyses for RNA-sequencing and microarray studies. *Nucleic Acids Res.* **43**, e47 (2015).
21. W. E. Johnson, C. Li, A. Rabinovic, Adjusting batch effects in microarray expression data using empirical bayes methods. *Biostatistics* **8**, 118–127 (2007).
22. Y. Zhang, G. Parmigiani, W. E. Johnson, ComBat-seq: Batch effect adjustment for RNA-seq count data. *NAR Genom Bioinform.* **2**, lqaa078 (2020).
23. L. Haghverdi, A. T. L. Lun, M. D. Morgan, J. C. Marioni, Batch effects in single-cell RNA-sequencing data are corrected by matching mutual nearest neighbors. *Nat. Biotechnol.* **36**, 421–427 (2018).
24. C. B. Azodi, L. Zappia, A. Oshlack, D. J. McCarthy, splatPop: Simulating population scale single-cell RNA sequencing data. *Genome Biol.* **22.1**, 1–16 (2021).
25. L. Zappia, B. Phipson, A. Oshlack, Splatter: Simulation of single-cell RNA sequencing data. *Genome Biol.* **18**, 174 (2017).
26. A. Kamburov, U. Stelzl, H. Lehrach, R. Herwig, The ConsensusPathDB interaction database: 2013 update. *Nucleic Acids Res.* **41**, D793–D800 (2013).
27. Z. Hu, M. Artibani, A. Alsaadi, N. Wietek, M. Morotti, T. Shi, Z. Zhong, L. S. Gonzalez, S. El-Sahhar, M. KaramiNejadRanjbar, G. Mallett, Y. Feng, K. Masuda, Y. Zheng, K. Chong, S. Damato, S. Dhar, L. Campo, R. G. Campanile, H. S. Majd, V. Rai, D. Maldonado-Perez, S. Jones, V. Cerundolo, T. Sauka-Spengler, C. Yau, A. A. Ahmed, The repertoire of serous ovarian cancer non-genetic heterogeneity revealed by single-cell sequencing of normal fallopian tube epithelial cells. *Cancer Cell* **37**, 226–242.e7 (2020).
28. B. Izar, I. Tirosh, E. H. Stover, I. Wakiro, M. S. Cuoco, I. Alter, C. Rodman, R. Leeson, M.-J. Su, P. Shah, M. Iwanicki, S. R. Walker, A. Kanodia, J. C. Melms, S. Mei, J.-R. Lin, C. B. M. Porter, M. Slyper, J. Waldman, L. Jerby-Arnon, O. Ashenberg, T. J. Brinker, C. Mills, M. Rogava, S. Vigneau, P. K. Sorger, L. A. Garraway, P. A. Konstantinopoulos, J. F. Liu, U. Matulonis, B. E. Johnson, O. Rozenblatt-Rosen, A. Rotem, A. Regev, A single-cell landscape of high-grade serous ovarian cancer. *Nat. Med.* **26**, 1271–1279 (2020).
29. S. M. Harrison, E. R. Riggs, D. R. Maglott, J. M. Lee, D. R. Azzariti, A. Niehaus, E. M. Ramos, C. L. Martin, M. J. Landrum, H. L. Rehm, Using clinvar as a resource to support variant interpretation. *Curr. Protoc. Hum. Genet.* **89**, 8.16.1–8.16.23 (2016).
30. T. Tickle, G. C. Ti, M. Brown, B. Haas, inferCNV of the Trinity CTAT Project (Klarman Cell Observatory, Broad Institute of MIT and Harvard, 2019); https://github.com/broadinstitute/inferCNV.
31. A. Häkkinen, K. Zhang, A. Alkodsi, N. Andersson, E. P. Erkan, J. Dai, K. Kaipio, T. Lamminen, N. Mansuri, K. Huhtinen, A. Vähärautio, O. Carpén, J. Hynninen, S. Hietanen, R. Lehtonen, S. Hautaniemi, PRISM: Recovering cell-type-specific expression profiles from individual composite RNA-seq samples. *Bioinformatics* **37**, 2882–2888 (2021).
32. A.-M. Patch, E. L. Christie, D. Etemadmoghadam, D. W. Garsed, J. George, S. Fereday, K. Nones, P. Cowin, K. Alsop, P. J. Bailey, K. S. Kassahn, F. Newell, M. C. J. Quinn, S. Kazakoff, K. Quek, C. Wilhelm-Benartzi, E. Curry, H. S. Leong; Australian ovarian cancer study group, A. Hamilton, L. Mileshkin, G. Au-Yeung, C. Kennedy, J. Hung, Y.-E. Chiew, P. Harnett, M. Friedlander, M. Quinn, J. Pyman, S. Cordner, P. O'Brien, J. Leditschke, G. Young, K. Strachan, P. Waring, W. Azar, C. Mitchell, N. Traficante, J. Hendley, H. Thorne, M. Shackleton, D. K. Miller, G. M. Arnau, R. W. Tothill, T. P. Holloway, T. Semple, I. Harliwong, C. Nourse, E. Nourbakhsh, S. Manning, S. Idrisoglu, T. J. C. Bruxner, A. N. Christ, B. Poudel, O. Holmes, M. Anderson, C. Leonard, A. Lonie, N. Hall, S. Wood, D. F. Taylor, Q. Xu, J. L. Fink, N. Waddell, R. Drapkin, E. Stronach, H. Gabra, R. Brown, A. Jewell, S. H. Nagaraj, E. Markham, P. J. Wilson, J. Ellul, O. McNally, M. A. Doyle, R. Vedururu, C. Stewart, E. Lengyel, J. V. Pearson, N. Waddell, A. de Fazio, S. M. Grimmond, D. D. L. Bowtell, Whole-genome characterization of chemoresistant ovarian cancer. *Nature* **527**, 398 (2015).
33. L. B. Alexandrov, S. Nik-Zainal, D. C. Wedge, S. A. J. R. Aparicio, S. Behjati, A. V. Biankin, G. R. Bignell, N. Bolli, A. Borg, A.-L. Børresen-Dale, S. Boyault, B. Burkhardt, A. P. Butler, C. Caldas, H. R. Davies, C. Desmedt, R. Eils, J. E. Eyfjörd, J. A. Foekens, M. Greaves, F. Hosoda, B. Hutter, T. Ilicic, S. Imbeaud, M. Imielinski, N. Jäger, D. T. W. Jones, D. Jones, S. Knappskog, M. Kool, S. R. Lakhani, C. López-Otín, S. Martin, N. C. Munshi, H. Nakamura, P. A. Northcott, M. Pajic, E. Papaemmanuil, A. Paradiso, J. V. Pearson, X. S. Puente, K. Raine, M. Ramakrishna, A. L. Richardson, J. Richter, P. Rosenstiel, M. Schlesner, T. N. Schumacher, P. N. Span, J. W. Teague, Y. Totoki, A. N. J. Tutt, R. Valdés-Mas, M. M. van Buuren, L. van 't Veer, A. Vincent-Salomon, N. Waddell, L. R. Yates; Australian Pancreatic Cancer Genome Initiative; ICGC Breast Cancer Consortium; ICGC MMML-Seq Consortium; ICGC

PedBrain, J. Zucman-Rossi, P. A. Futreal, U. McDermott, P. Lichter, M. Meyerson, S. M. Grimmond, R. Siebert, E. Campo, T. Shibata, S. M. Pfister, P. J. Campbell, M. R. Stratton, Signatures of mutational processes in human cancer. *Nature* **500**, 415–421 (2013).

34. M. Andreatta, J. Corria-Osorio, S. Müller, R. Cubas, G. Coukos, S. J. Carmona, Interpretation of T cell states from single-cell transcriptomics data using reference atlases. *Nat. Commun.* **12**, 2965 (2021).

35. L. T. Roumenina, M. V. Daugan, R. Noé, F. Petitprez, Y. A. Vano, R. Sanchez-Salas, E. Becht, J. Meilleroux, B. L. Clec'h, N. A. Giraldo, N. S. Merle, C.-M. Sun, V. Verkarre, P. Validire, J. Selves, L. Lacroix, O. Delfour, I. Vandenberghe, C. Thuilliez, S. Keddani, I. B. Sakhi, E. Barret, P. Ferré, N. Corvaïa, A. Passioukov, E. Chetaille, M. Botto, A. de Reynies, S. M. Oudard, A. Mejean, X. Cathelineau, C. Sautès-Fridman, W. H. Fridman, Tumor cells hijack macrophage-produced complement C1q to promote tumor growth. *Cancer Immunol. Res.* **7**, 1091–1105 (2019).

36. Y. Katzenelenbogen, F. Sheban, A. Yalin, I. Yofe, D. Svetlichnyy, D. A. Jaitin, C. Bornstein, A. Moshe, H. Keren-Shaul, M. Cohen, S.-Y. Wang, B. Li, E. David, T.-M. Salame, A. Weiner, I. Amit, Coupled scRNA-seq and intracellular protein activity reveal an immunosuppressive role of TREM2 in cancer. *Cell* **182**, 872–885.e19 (2020).

37. D. Öhlund, A. Handly-Santana, G. Biffi, E. Elyada, A. S. Almeida, M. Ponz-Sarvise, V. Corbo, T. E. Oni, S. A. Hearn, E. J. Lee, I. I. C. Chio, C.-I. Hwang, H. Tiriac, L. A. Baker, D. D. Engle, C. Feig, A. Kultti, M. Egeblad, D. T. Fearon, J. M. Crawford, H. Clevers, Y. Park, D. A. Tuveson, Distinct populations of inflammatory fibroblasts and myofibroblasts in pancreatic cancer. *J. Exp. Med.* **214**, 579–596 (2017).

38. G. Biffi, T. E. Oni, B. Spielman, Y. Hao, E. Elyada, Y. Park, J. Preall, D. A. Tuveson, IL1-induced JAK/STAT signaling is antagonized by TGFβ to shape CAF heterogeneity in pancreatic ductal adenocarcinoma. *Cancer Discov.* **9**, 282–301 (2019).

39. D. Duluc, Y. Delneste, F. Tan, M.-P. Moles, L. Grimaud, J. Lenoir, L. Preisser, I. Anegon, L. Catala, N. Ifrah, P. Descamps, E. Gamelin, H. Gascan, M. Hebbar, P. Jeannin, Tumor-associated leukemia inhibitory factor and IL-6 skew monocyte differentiation into tumor-associated macrophage-like cells. *Blood* **110**, 4319–4330 (2007).

40. K. R. Jordan, M. J. Sikora, J. E. Slansky, A. Minic, J. K. Richer, M. R. Moroney, J. Hu, R. J. Wolsky, Z. L. Watson, T. M. Yamamoto, J. C. Costello, A. Clauset, K. Behbakht, T. R. Kumar, B. G. Bitler, The capacity of the ovarian cancer tumor microenvironment to integrate inflammation signaling conveys a shorter disease-free interval. *Clin. Cancer Res.* **26**, 6362–6373 (2020).

41. S. C. van den Brink, F. Sage, Á. Vértesy, B. Spanjaard, J. Peterson-Maduro, C. S. Baron, C. Robin, A. van Oudenaarden, Single-cell sequencing reveals dissociation-induced gene expression in tissue subpopulations. *Nat. Methods* **14**, 935–936 (2017).

42. H. Cui, M. Guo, D. Xu, Z.-C. Ding, G. Zhou, H.-F. Ding, J. Zhang, Y. Tang, C. Yan, The stress-responsive gene ATF3 regulates the histone acetyltransferase Tip60. *Nat. Commun.* **6**, 6752 (2015).

43. K. C. Valkenburg, A. E. de Groot, K. J. Pienta, Targeting the tumour stroma to improve cancer therapy. *Nat. Rev. Clin. Oncol.* **15**, 366–381 (2018).

44. E. Lou, R. I. Vogel, S. Hoostal, M. Klein, M. A. Linden, D. Teoh, M. A. Geller, Tumor-stroma proportion as a predictive biomarker of resistance to platinum-based chemotherapy in patients with ovarian cancer. *JAMA Oncol.* **5**, 1222–1224 (2019).

45. R. Moncada, D. Barkley, F. Wagner, M. Chiodin, J. C. Devlin, M. Baron, C. H. Hajdu, D. M. Simeone, I. Yanai, Integrating microarray-based spatial transcriptomics and single-cell RNA-seq reveals tissue architecture in pancreatic ductal adenocarcinomas. *Nat. Biotechnol.* **38**, 333–342 (2020).

46. I. Wertel, D. Suszczyk, A. Pawłowska, M. Bilska, A. Chudzik, W. Skiba, R. Paduch, J. Kotarski, Prognostic and clinical value of interleukin 6 and CD45$^+$CD14$^+$ inflammatory cells with PD-L1$^+$/PD-L2$^+$ expression in patients with different manifestation of ovarian cancer. *J. Immunol. Res.* **2020**, 1715064 (2020).

47. A. Alvarez Secord, K. Bell Burdett, K. Owzar, D. Tritchler, A. B. Sibley, Y. Liu, M. D. Starr, J. C. Brady, H. A. Lankes, H. I. Hurwitz, R. S. Mannel, K. S. Tewari, D. M. O'Malley, H. Gray, J. N. Bakkum-Gamez, K. Fujiwara, M. Boente, W. Deng, R. A. Burger, M. J. Birrer, A. B. Nixon, Predictive blood-based biomarkers in patients with epithelial ovarian cancer treated with carboplatin and paclitaxel with or without bevacizumab: Results from GOG-0218. *Clin. Cancer Res.* **26**, 1288–1296 (2020).

48. M. Baron, M. Tagore, M. V. Hunter, I. S. Kim, R. Moncada, Y. Yan, N. R. Campbell, R. M. White, I. Yanai, The stress-like cancer cell state is a consistent component of tumorigenesis. *Cell Syst.* **11**, 536–546.e7 (2020).

49. D. Huang, J. Xue, S. Li, D. Yang, Oxaliplatin and infliximab synergize to induce regression of colon cancer. *Oncol. Lett.* **15**, 1517–1522 (2018).

50. K. B. Long, G. Tooker, E. Tooker, S. L. Luque, J. W. Lee, X. Pan, G. L. Beatty, IL6 receptor blockade enhances chemotherapy efficacy in pancreatic ductal adenocarcinoma. *Mol. Cancer Ther.* **16**, 1898–1908 (2017).

51. D. Høgdall, C. J. O'Rourke, C. Dehlendorff, O. F. Larsen, L. H. Jensen, A. Z. Johansen, H. Dang, V. M. Factor, M. Grunnet, M. Mau-Sørensen, D. V. N. P. Oliveira, D. Linnemann, M. K. Boisen, X. W. Wang, J. S. Johansen, J. B. Andersen, Serum IL6 as a prognostic biomarker and IL6R as a therapeutic target in biliary tract cancers. *Clin. Cancer Res.* **26**, 5655–5667 (2020).

52. M. Lecavalier-Barsoum, N. Chaudary, K. Han, M. Pintilie, R. P. Hill, M. Milosevic, Targeting CXCL12/CXCR4 and myeloid cells to improve the therapeutic ratio in patient-derived cervical cancer models treated with radio-chemotherapy. *Br. J. Cancer* **121**, 249–256 (2019).

53. K. Melgar, M. M. Walker, L. M. Jones, L. C. Bolanos, K. Hueneman, M. Wunderlich, J.-K. Jiang, K. M. Wilson, X. Zhang, P. Sutter, A. Wang, X. Xu, K. Choi, G. Tawa, D. Lorimer, J. Abendroth, E. O'Brien, S. B. Hoyt, E. Berman, C. A. Famulare, J. C. Mulloy, R. L. Levine, J. P. Perentesis, C. J. Thomas, D. T. Starczynowski, Overcoming adaptive therapy resistance in AML by targeting immune response pathways. *Sci. Transl. Med.* **11**, eaaw8828 (2019).

54. B. Dave, M. D. Landis, D. J. Tweardy, J. C. Chang, L. E. Dobrolecki, M.-F. Wu, X. Zhang, T. F. Westbrook, S. G. Hilsenbeck, D. Liu, M. T. Lewis, Selective small molecule Stat3 inhibitor reduces breast cancer tumor-initiating cells and improves recurrence free survival in a human-xenograft model. *PLOS ONE* **7**, e30207 (2012).

55. H. Torrey, J. Butterworth, T. Mera, Y. Okubo, L. Wang, D. Baum, A. Defusco, S. Plager, S. Warden, D. Huang, E. Vanamee, R. Foster, D. L. Faustman, Targeting TNFR2 with antagonistic antibodies inhibits proliferation of ovarian cancer cells and tumor-associated Tregs. *Sci. Signal.* **10**, eaaf8608 (2017).

56. Y. Zeng, B. Li, Y. Liang, P. M. Reeves, X. Qu, C. Ran, Q. Liu, M. V. Callahan, A. E. Sluder, J. A. Gelfand, H. Chen, M. C. Poznansky, Dual blockade of CXCL12-CXCR4 and PD-1-PD-L1 pathways prolongs survival of ovarian tumor-bearing mice by prevention of immunosuppression in the tumor microenvironment. *FASEB J.* **33**, 6596–6608 (2019).

57. T. H. Kim, X. Zhou, M. Chen, Demystifying "drop-outs" in single-cell UMI data. *Genome Biol.* **21**, 196 (2020).

58. V. Svensson, Droplet scRNA-seq is not zero-inflated. *Nat. Biotechnol.* **38**, 147–150 (2020).

59. A. Sarkar, M. Stephens, Separating measurement and expression models clarifies confusion in single-cell RNA sequencing analysis. *Nat. Genet.* **53**, 770–777 (2021).

60. A. P. Dempster, N. M. Laird, D. B. Rubin, Maximum likelihood from incomplete data via the EM Algorithm. *J. R. Stat. Soc. B. Methodol.* **39**, 1–38 (1977).

61. H. T. N. Tran, K. S. Ang, M. Chevrier, X. Zhang, N. Y. S. Lee, M. Goh, J. Chen, A benchmark of batch-effect correction methods for single-cell RNA sequencing data. *Genome Biol.* **21**, 12 (2020).

62. M. Baron, A. Veres, S. L. Wolock, A. L. Faust, R. Gaujoux, A. Vetere, J. H. Ryu, B. K. Wagner, S. S. Shen-Orr, A. M. Klein, D. A. Melton, I. Yanai, A single-cell transcriptomic map of the human and mouse pancreas reveals inter- and intra-cell population structure. *Cell Syst.* **3**, 346–360.e4 (2016).

63. M. J. Muraro, G. Dharmadhikari, D. Grün, N. Groen, T. Dielen, E. Jansen, L. van Gurp, M. A. Engelse, F. Carlotti, E. J. P. de Koning, A. van Oudenaarden, A single-cell transcriptome atlas of the human pancreas. *Cell Syst.* **3**, 385–394.e3 (2016).

64. Å. Segerstolpe, A. Palasantza, P. Eliasson, E.-M. Andersson, A.-C. Andréasson, X. Sun, S. Picelli, A. Sabirsh, M. Clausen, M. K. Bjursell, D. M. Smith, M. Kasper, C. Ämmälä, R. Sandberg, Single-cell transcriptome profiling of human pancreatic islets in health and type 2 diabetes. *Cell Metab.* **24**, 593–607 (2016).

65. Y. J. Wang, J. Schug, K.-J. Won, C. Liu, A. Naji, D. Avrahami, M. L. Golson, K. H. Kaestner, Single-cell transcriptomics of the human endocrine pancreas. *Diabetes* **65**, 3028–3038 (2016).

66. Y. Xin, J. Kim, H. Okamoto, M. Ni, Y. Wei, C. Adler, A. J. Murphy, G. D. Yancopoulos, C. Lin, J. Gromada, RNA sequencing of single human islet cells reveals type 2 diabetes genes. *Cell Metab.* **24**, 608–615 (2016).

67. D. J. McCarthy, K. R. Campbell, A. T. L. Lun, Q. F. Wills, Scater: Pre-processing, quality control, normalization and visualization of single-cell RNA-seq data in R. *Bioinformatics* **33**, 1179–1186 (2017).

68. J. T. Leek, W. E. Johnson, H. S. Parker, E. J. Fertig, A. E. Jaffe, J. D. Storey, Y. Zhang, L. C. Torres, sva: Surrogate variable analysis. *R package version.* **3**, 882–883 (2019).

69. V. D. Blondel, J.-L. Guillaume, R. Lambiotte, E. Lefebvre, Fast unfolding of communities in large networks. *J. Stat. Mech.* **2008**, P10008 (2008).

70. L. Hubert, P. Arabie, Comparing partitions. *J. Class.* **2**, 193–218 (1985).

71. L. Scrucca, M. Fop, T. B. Murphy, A. E. Raftery, Mclust 5: Clustering, classification and density estimation using Gaussian finite mixture models. *R J.* **8**, 289–317 (2016).

72. P. Pons, M. Latapy, Computing communities in large networks using random walks. in *Computer and Information Sciences - ISCIS 2005*, Yolum, T. Güngör, F. Gürgen, C. Özturan, Eds. (Springer, 2005), pp. 284-293.

73. P. S. Bhatia, S. Iovleff, G. Govaert, blockcluster: An R package for model-based co-clustering. *J. Stat. Softw.* **76**, 1–24 (2017).

74. D. A. Barbie, P. Tamayo, J. S. Boehm, S. Y. Kim, S. E. Moody, I. F. Dunn, A. C. Schinzel, P. Sandy, E. Meylan, C. Scholl, S. Fröhling, E. M. Chan, M. L. Sos, K. Michel, C. Mermel, S. J. Silver, B. A. Weir, J. H. Reiling, Q. Sheng, P. B. Gupta, R. C. Wadlow, H. Le, S. Hoersch, B. S. Wittner, S. Ramaswamy, D. M. Livingston, D. M. Sabatini, M. Meyerson, R. K. Thomas,

E. S. Lander, J. P. Mesirov, D. E. Root, D. G. Gilliland, T. Jacks, W. C. Hahn, Systematic RNA interference reveals that oncogenic KRAS-driven cancers require TBK1. *Nature* **462**, 108–112 (2009).

75. C. McQuin, A. Goodman, V. Chernyshev, L. Kamentsky, B. A. Cimini, K. W. Karhohs, M. Doan, L. Ding, S. M. Rafelski, D. Thirstrup, W. Wiegraebe, S. Singh, T. Becker, J. C. Caicedo, A. E. Carpenter, CellProfiler 3.0: Next-generation image processing for biology. *PLOS Biol.* **16**, e2005970 (2018).
76. M. A. Durante, D. A. Rodriguez, S. Kurtenbach, J. N. Kuznetsov, M. I. Sanchez, C. L. Decatur, H. Snyder, L. G. Feun, A. S. Livingstone, J. W. Harbour, Single-cell analysis reveals new evolutionary complexity in uveal melanoma. *Nat. Commun.* **11**, 496 (2020).
77. C. Li, B. Liu, B. Kang, Z. Liu, Y. Liu, C. Chen, X. Ren, Z. Zhang, SciBet as a portable and fast single cell type identifier. *Nat. Commun.* **11**, 1818 (2020).
78. J. Cao, M. Spielmann, X. Qiu, X. Huang, D. M. Ibrahim, A. J. Hill, F. Zhang, S. Mundlos, L. Christiansen, F. J. Steemers, C. Trapnell, J. Shendure, The single-cell transcriptional landscape of mammalian organogenesis. *Nature* **566**, 496–502 (2019).
79. R. Browaeys, W. Saelens, Y. Saeys, NicheNet: Modeling intercellular communication by linking ligands to target genes. *Nat. Methods* **17**, 159–162 (2020).

Acknowledgments: The results published here are in part based on data generated by TCGA managed by the NCI and NHGRI. Information about TCGA can be found at https://cancergenome.nih.gov/. scRNA-seq was performed at Jussi Taipale Lab, Karolinska Institute, Sweden and Institute for Molecular Medicine Finland, Finland. Figure 1A was created with Biorender.com. **Funding:** This work was supported by the European Union's Horizon 2020 research and innovation programme under grant agreement no. 667403 for HERCULES (Comprehensive Characterization and Effective Combinatorial Targeting of High-Grade Serous Ovarian Cancer via Single-Cell Analysis), European Union's Horizon 2020 research and innovation programme under grant agreement no. 965193 for DECIDER (Clinical Decision via Integrating Multiple Data Levels to Overcome Chemotherapy Resistance in High-Grade Serous Ovarian Cancer), the Academy of Finland (project no. 344697) for Era PerMed JTC2020 project PARIS (Precision drugs Against Resistance In Subpopulations), the Academy of Finland (project nos. 325956, 289059, 322927, 294023, and 319243), and the Sigrid Jusélius Foundation the Cancer Foundation Finland. **Author contributions:** Conceptualization: K.Z., J.O., A.H., S.Ha., and A.Vä. Methodology and software: K.Z. and A.H. Formal analysis: K.Z., S.J., and A.H. Validation: S.J., N.A., and K.H. Investigation: K.Z., E.P.E., J.D., N.A., S.J., K.K., T.L., N.M., K.H., A.Vi., A.H., S.Ha., and A.Vä. Resources: K.K., T.L., N.M., K.H., O.C., J.H., S.Hi., S.Ha., and A.Vä. Data curation: K.Z., E.P.E., J.H., A.Vi., S.Ha., and A.Vä. Visualization: K.Z. and E.P.E. Supervision: A.H., S.Ha., and A.Vä. Project administration: S.Ha. and A.Vä. Funding acquisition: O.C., S.Hi., J.H., S.Ha., and A.Vä. Writing—original draft: K.Z., S.Ha., and A.Vä. Writing—review and editing: K.Z., E.P.E., J.D., N.A., S.J., K.K., T.L., N.M., K.H., O.C., S.Hi., J.O., J.H., A.Vi., A.H., S.Ha., and A.Vä. **Competing interests:** The authors declare that they have no competing interests. **Data and materials availability:** All data needed to evaluate the conclusions in the paper are present in the paper and/or the Supplementary Materials. Additional data related to this paper may be requested from the authors. Raw scRNA-seq data (accession code EGAS00001005010) and raw bulk RNA-seq data (EGAS00001004714) are deposited in the European Genome-phenome Archive (EGA). Count data from scRNA-seq are available in Gene Expression Omnibus (GEO) with accession code GSE165897. The source code for PRIMUS is available at GitHub (https://github.com/KaiyangZ/PRIMUS) and Zenodo (https://doi.org/10.5281/zenodo.5800128).

Submitted 1 September 2021
Accepted 25 December 2021
Published 23 February 2022
10.1126/sciadv.abm1831

Science Advances

Longitudinal single-cell RNA-seq analysis reveals stress-promoted chemoresistance in metastatic ovarian cancer

Kaiyang ZhangErdogan Pekcan ErkanSanaz JamalzadehJun DaiNoora AnderssonKatja KaipioTarja LamminenNaziha MansuriKaisa HuhtinenOlli CarpénSakari HietanenJaana OikkonenJohanna HynninenAnni VirtanenAntti HäkkinenSampsa HautaniemiAnna Vähärautio

Sci. Adv., 8 (8), eabm1831. • DOI: 10.1126/sciadv.abm1831

Science Advances (ISSN) is published by the American Association for the Advancement of Science. 1200 New York Avenue NW, Washington, DC 20005. The title *Science Advances* is a registered trademark of AAAS.